Mathematical Modeling of the Melt Pool During a Physical Vapor Deposition Process

by

Daniel H. Simon

B.S. Mechanical Engineering (1996)
Rutgers University

Submitted to the Department of Mechanical Engineering
in Partial Fulfillment of the Requirements for the Degree of
Master of Science in Mechanical Engineering

at the

Massachusetts Institute of Technology

February 1998

Signature of Author _____
Department of Mechanical Engineering
December 16, 1997

Certified by _____
Uday Pal
Associate Professor of Materials Science and Engineering
Thesis Supervisor

Certified by _____
Roger Kamm
Professor of Mechanical Engineering
Department Reader

Accepted by _____
Ain A Sonin
Chairman, Department Committee on Graduate Students

Acknowledgements

I would like to dedicate this work to my caring, supportive, and devoted wife, Amy. I would also like to thank my parents and family for their continued encouragement throughout my education. In addition, I would like to thank Professors Uday Pal and Roger Kamm for their time, expertise, and guidance.

Table of Contents:

Mathematical Modeling of the Melt Pool During
a Physical Vapor Deposition Process
by
Daniel H. Simon

Submitted to the Department of Mechanical Engineering
on December 16, 1997 in Partial Fulfillment of the
Requirements for the Degree of Master of Science in
Mechanical Engineering

Abstract

The molten pool of source material in a Physical Vapor Deposition Process is the subject of analysis in this thesis. A model of the melt pool and the ingot below is generated in an effort to study the fluid flow and heat transfer within the pool. This model incorporates all of the following mechanisms for heat transfer into and out of the melt pool/ingot system: electron-beam impingement upon the melt pool surface, absorption of latent heat of evaporation at the melt pool surface, radiation from the melt pool surface, loss of sensible heat carried off with the vapor, cooling by the crucible containing the melt pool/ingot. Fluid flow within the melt pool model is driven by both natural convection and by surface tension gradients on the melt pool surface. Due to the complexity of the differential equations and boundary equations governing the model, this detailed study is performed through a finite element analysis.

In an effort to better understand and, eventually, control the entire PVD process, the temperature distribution and fluid flow within the melt pool are studied under varying sets of operating conditions. Reduced order models of the system are generated from this analysis. In order to generate these models, several key features of the melt pool are selected to represent the state of the system. The features chosen are of importance to subsequent studies aimed at controlling the remainder of the PVD process. It is proposed that these three features be selected: the average melt pool surface temperature, the difference between the melt pool pool's maximum and minimum surface temperatures, and the average vapor flow rate from the melt pool. The reduced order models generated by this study predict the dependencies of these quantities upon the controllable features of the melt pool (e.g. the beam power incident upon the ingot and the scan pattern used to deliver this power). Additionally, an error analysis is performed to place bounds upon the error introduced into these models by uncertainty in the thermophysical property data used to generate them. The results generated by this thesis need to be incorporated into separate studies vapor transport and deposition processes in order to attain an understanding of the entire PVD process.

TABLE OF SYMBOLS

Symbol	Definition	Units
A	Ingot Cross Sectional Area	m^2
α	Thermal Diffusivity	$m^2 s^{-1}$
B(r)	Beam Heat Flux Distribution	$W m^{-2}$
β	Volume Expansion Coefficient	K^{-1}
c_p	Specific Heat	$J kg^{-1} K^{-1}$
ε	Radiative Emissivity	-
$F_{pattern}$	Fraction of Beam Power on Ingot	-
$F_{scatter}$	Fraction of Non-scattered Electrons	-
Φ	Viscous Dissipation Function	$W m^{-3}$
Gr	Grashof Number	-
g	Gravitational Acceleration	$m s^{-2}$
h	Specific Enthalpy	$J kg^{-1}$
h_c	Heat Transfer Coefficient	$W m^{-2} K^{-1}$
h_{lv}	Latent Heat of Vaporization	$J kg^{-1}$
h_{sl}	Latent Heat of Melting	$J kg^{-1}$
J	Evaporative Flux	$mol m^{-2} s^{-1}$
k	Thermal Conductivity	$W m^{-1} K^{-1}$
L	Characteristic Length	m
M_i	Molar Mass of species i	$kg mol^{-1}$
$\dot{m}$	Mass Flow Rate	$kg s^{-1}$
$\dot{m}^*$	Dimensionless Form of $\dot{m}$	-
μ	Viscosity	$kg m^{-1} s^{-1}$
n_i	Component of Normal Vector in i direction	-
Nu_{hc}	Nusselt Number based on h_c	-
Nu_q	Nusselt Number based on q	-
P	Beam Power	W
P	Ingot Perimeter	m
Pr	Prandtl Number	-
p	Pressure	Pa
p_v	Vapor Pressure	Pa
q	Heat Flux	$W m^{-2}$
θ	Dimensionless Temperature	-
θ_{avg}	Dimensionless Form of T_{avg}	-
$\Delta\theta_{surf}$	Dimensionless Form of ΔT_{surf}	-
R_u	Universal Gas Constant	$J mol^{-1} K^{-1}$
R	Ingot Radius	m
r	Radial Distance	m
r*	Dimensionless Radial Distance	-
ρ	Density	$kg m^{-3}$
St	Dimensionless Surface Tension Number	-
σ	Surface Tension	$N m^{-1}$
σ	Gaussian Standard Deviation	m
σ^*	Dimensionless Standard Deviation	-

σ_o	Stefan-Boltzman constant	$W\ m^{-2}\ K^{-4}$
T	Temperature	K
T_{avg}	Average Pool Surface	K
ΔT_{surf}	Difference Between Minimum and Maximum Pool Surface Temperatures	K
t	Time	s
τ_{ij}	i,j Component of Shear Stress	Pa
u_i	Flow Velocity in i Direction	$m\ s^{-1}$
V	Ingot Feed Rate	$m\ s^{-1}$
z	Vertical Distance	m

Chapter 1.0 Introduction

Physical vapor deposition (PVD) is one of several methods currently used to apply thermal barrier coatings (TBCs) to aircraft components subjected to high temperature environments. In this process, a heat source is directed onto a supply of the TBC material creating a molten pool. The material then evaporates into the vacuum of the surrounding deposition chamber creating a vapor cloud. The hardware to be coated is positioned inside the chamber above the molten pool where the material is deposited by condensation.

PVD is performed using many different hardware configurations. This thesis shall consider one particular configuration currently used by Chromalloy Turbine Technologies in Middletown, NY. The particular example of PVD to be studied is shown in Figure 1-1. The heat source is a scanning electron beam generated by a 270° electron-beam gun. The supply of TBC material is an ingot of Yttria stabilized Zirconia (YSZ). The gun is positioned below the deposition chamber which contains the hardware to be coated and the upper surface of the ingot. Electromagnets are used to deflect the beam so that it strikes the ingot's upper surface. The electron beam is traced rapidly over the top surface of the ingot such that it melts and evaporates. To maintain a supply of YSZ for a prolonged deposition process, the ingot is fed continuously upwards through a water-cooled copper crucible. The hardware being coated is rotated above the melt pool to promote uniform coatings. To control the temperature of the hardware being coated, an over-source heater is used. This heater is found at the top of the coating chamber.

Of interest to the PVD industry is attaining better control over this process. It is known that the microstructural characteristics of TBCs vary according to the conditions they are manufactured under. Further, it is understood that TBCs with certain microstructures are more effective and reliable. Two of the most important process parameters that impact TBC microstructure are the temperature of the hardware being coated and the mass flux of source material impinging upon the hardware. Consequently, it is highly desirable to be able to control these parameters during TBC production.

Past attempts at the control of this process have been based upon the statistical analysis of coatings fabricated under various conditions. This approach has allowed coating manufacturers to develop a set of bounds on their process parameters inside which they can expect to produce acceptable TBCs. To some degree, this approach has also allowed these manufacturers to optimize their process parameters. To move to the next level of process control, a better understanding of the process is needed first. The need for this understanding is the motivation behind this research.

Figure 1-1: Schematic of the PVD process

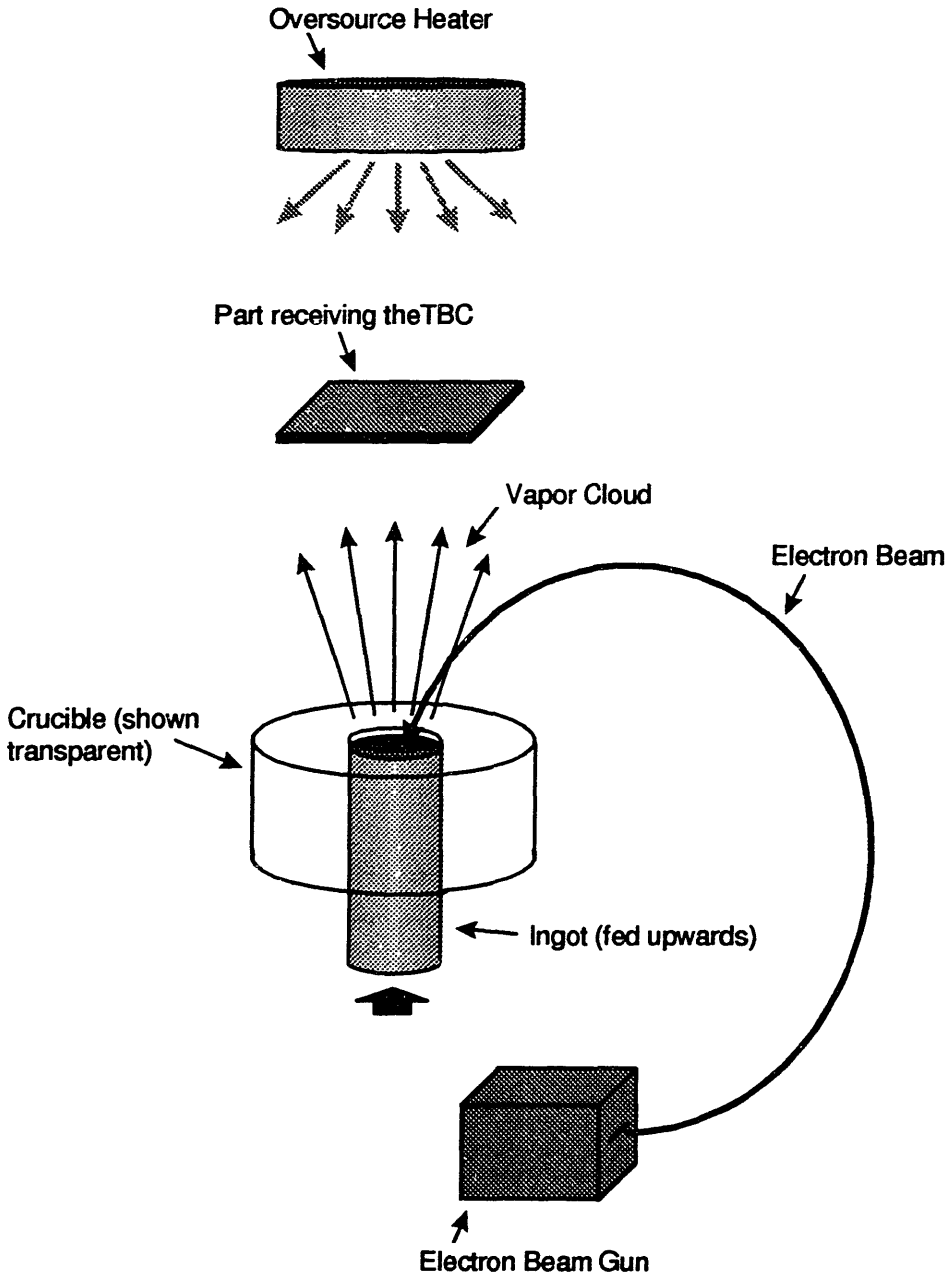

From the point of view of the source material, the PVD process can be broken down into three distinct stages: melting and evaporation, vapor transport, and deposition. Each of these stages is quite complex and suggests a different approach to detailed analysis (e.g. a finite element analysis for the melting and evaporation and a direct simulation monte carlo study for the vapor transport). This thesis deals with the first stage of the PVD process - the melting of the solid ingot and subsequent evaporation from the resulting molten pool.

A detailed study of the melt pool/ingot requires a thorough knowledge of the thermophysical properties of YSZ in both its solid and liquid states. A thorough literature search was performed to obtain these properties. In its solid state, the properties of YSZ have been well studied. In its liquid state, YSZ breaks down into its constituent species, Zirconia (ZrO_2) and Yttria (Y_2O_3). Unfortunately, very little information about the properties of Zirconia and Yttria in their liquid states is available. Since the YSZ of interest in this study contains only 7% Yttria by mass, we shall neglect the effect of Yttria on the thermophysical properties of the melt pool and consider instead a pool of pure molten Zirconia. In instances where the properties of Zirconia are unknown, the properties of Alumina have been substituted in their place. The substitution of Alumina's thermophysical properties for Zirconia's is commonly done in process modeling and should provide a reasonable approximation to the actual behavior of Zirconia. Appendix A contains a summary of the thermophysical properties used in this study.

After completing a study of the system's thermophysical properties, a thorough analysis is performed through a solution of the equations of conservation of mass, momentum, and energy. In this particular system, fluid motion and temperature distribution are tightly coupled. In addition, the boundary conditions on the melt pool's free surface consist of complex temperature dependent relations. These factors make an analytical solution of the governing equations quite impossible. Instead, a numerical solution must be obtained through an appropriate iterative procedure. As so, the quantitative results in this thesis shall be based upon a finite element analysis of the melt pool and ingot.

Chapter 2.0 Modeling

In order to study the melting and evaporation processes, we must develop an accurate model of the melt pool/ingot system. This model must contain all the essential features of the actual system. At the same time we must keep in mind that this system shall ultimately be subjected to a finite element analysis. As such, the model should be simple enough so that our computational demands do not become excessive. Essentially, we must balance our needs for accurate and timely results.

Discussion of Melt Pool/Ingot Features

Development of any model is begun by identifying and examining the actual system being studied. Our system shall be taken as a control volume enclosing the melt pool and an upper portion of the ingot. Figure 2-1 contains a detailed

Figure 2-1: Detailed Schematic of Melting and Evaporation Process

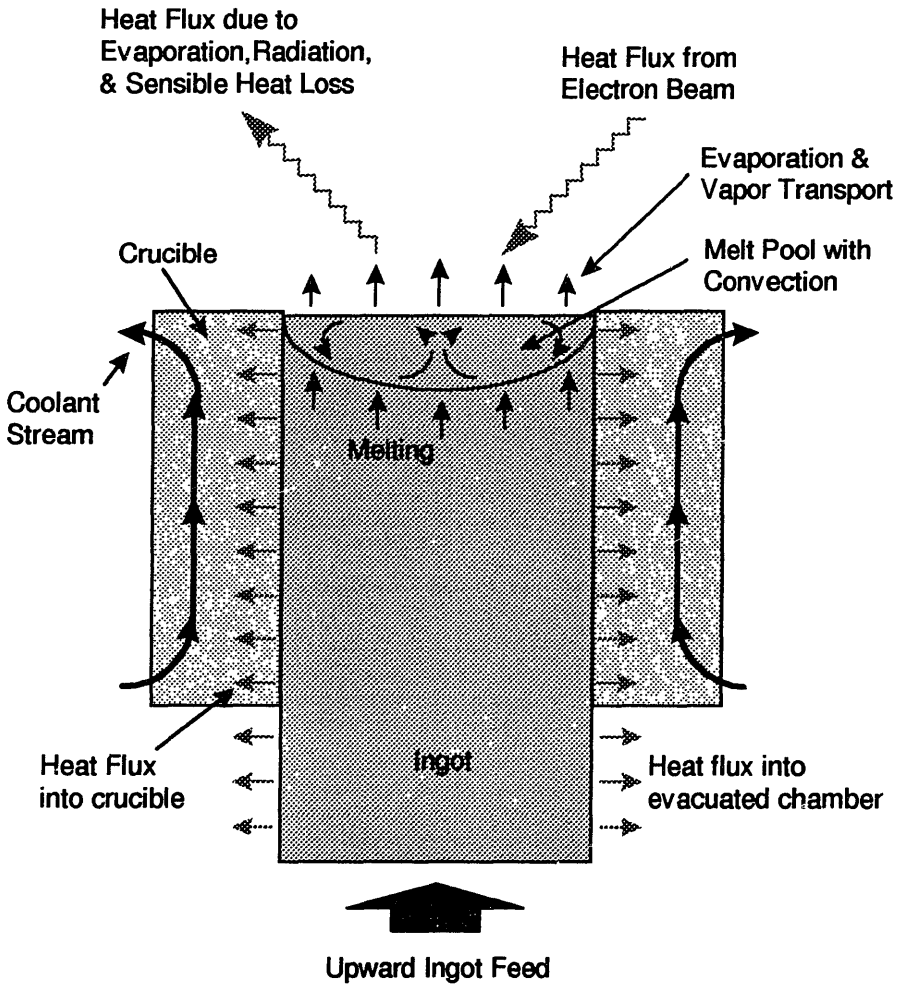

schematic of the system and the elements that interact with the system at its boundaries. The following paragraphs are devoted to a description of the melt pool and ingot.

There are numerous heat transfers between the system and its surroundings. The electron beam scans over the ingot's upper surface and provides a heat flux to the system. Heat flux out of the ingot's upper surface also occurs through radiation into the coating chamber, absorption of latent heat during evaporation, and the loss of sensible heat carried out with the hot vapor. Heat transfer occurs between the outer perimeter of the melt pool and ingot and the crucible which surrounds them. This transfer occurs by conduction across the tiny gap between the YSZ material and the crucible, by conduction through the crucible, and finally by forced convection into the crucible's coolant stream. Heat is also transferred from the lower portion of the ingot's perimeter directly into the evacuated chamber that contains it. This transfer is mainly by radiation. Finally, since heat transfer occurs by conduction throughout the ingot, additional heat transfer occurs out of the bottom of the system where the ingot is "cut".

Mass flux into and out of the chosen system occurs as well. The vapor emitted by the ingot's surface represents mass flux out of the system. A mass flux into the system is created by the upward motion of the ingot at the bottom of the control volume. These mass fluxes carry along with them sensible heat as well. The sensible heat carried off by the vapor is potentially large. However, the control volume is chosen to enclose enough of the ingot such that the temperature of the incoming ingot material is relatively low. This and the fact that the feed rate is also very slow will eventually lead us to neglect this sensible heat transfer.

Within the system there is further activity. Below the melting point of YSZ, the ingot remains solid and maintains a constant uniform velocity upwards. Once the melting point is reached, the ingot melts and absorbs energy in the latent heat of melting. The molten YSZ forms a liquid pool on top of the ingot as shown in Figure 2. Within this pool the fluid is mixed by natural convection. In addition, temperature gradients on the pool's free surface cause variations in surface tension. The resulting shear stresses on the pool's surface promote additional fluid motion

Symmetry

Having described the system completely, it is now possible to begin discussion of the model used in this research. It would be convenient to be able to model the system as an axisymmetric one. The electron-beam scanning pattern of the actual system being studied provides a nearly uniform heat transfer across the ingot's surface; therefore, when studying this pattern we shall model the electron-beam as a source of uniform heat flux on the pool's surface. When

studying the effect of alternate beam scan patterns we shall only consider patterns that would provide axisymmetric heat flux distributions.

The heat transfer between the melt pool/ingot and the crucible shall be modeled as purely convective with a single, uniform heat transfer coefficient. This assumption is probably poor since there would certainly be better thermal contact between the liquid YSZ and crucible than between the solid YSZ and crucible. However, it is certainly safe to assume that the crucible's cooling circuit is designed to provide nearly uniform heat transfer around the ingot's perimeter. Note that the assumption of purely convective heat transfer also disregards the radiative cooling occurring below the crucible. Regardless, it seems that the system can be satisfactorily modeled as axisymmetric system.

Steady State vs. Transient

While hardware is actually being coated in current PVD systems, these systems remain in a steady state. During initial transient period when the melt pool is first forming on top of the ingot, no hardware coating is done. The hardware to be coated does not enter the coating chamber until a steady state has been attained. Thus, the system shall be modeled as a steady state process.

Ingot Motion

With this assumption in mind, take note that the ingot feed rate will be an unknown before any detailed calculations are performed. In order to maintain a steady state, the feed rate must provide a mass flux that balances the mass flux out of the system due to evaporation. The evaporative mass flux will depend on the temperature of the melt pool's free surface while temperature is a quantity we will calculate using the model. To properly include the feed rate we should take an initial guess at this quantity and calculate the temperature distribution and mass fluxes across the pool's free surface. Then we could select a new feed rate based upon the calculated mass fluxes. This process would be iterated until the correct mass flux were determined.

If certain effects of the ingot motion were negligible, it would be possible to perform an analysis on the system using a stationary ingot. Consequently, it would not be necessary to perform the calculations mentioned above. The effects that must be considered are: the effect of the ingot's motion upon the system's temperature field, the effect of the energy consumed as latent heat at the melting front, the effect of the ingot's net upward motion on the melt pool velocities.

The power consumed per unit area due to the latent heat of melting is calculated according to:

$$q = \rho V h_{sl}$$

where q is the heat flux, ρ is density, V is the ingot feed rate, and h_{sl} is the latent heat of melting. Using the properties given in Appendix A for solid YSZ and a feed rate of 0.04 in/min (a typical value for industrial use) this heat flux would be ~10^4 W/m^2. Compare this value with an estimate of the axial heat flux through the ingot near the melting front calculated according to:

$$q = k\frac{\partial T}{\partial z} \sim k\frac{\Delta T_z}{\Delta z}$$

where ΔT_z is the temperature change between the pool's surface and the melting front, Δz is the pool depth, and k is the thermal conductivity of liquid Zirconia. Again using the properties in Appendix A, 100 K as an order of magnitude estimate for ΔT_z (thermal images of actual melt pool surfaces provide this estimate), and 1.0 mm as an order of magnitude estimate for Δz (examinations of discarded ingots with solidified pools provide this estimate), the estimated axial heat flux through the ingot would be ~10^5 W/m^2. Thus the axial heat flux through the melting front is an order of magnitude greater than the power absorbed per unit area due the latent heat of melting. Since the heat flux into the ingot equals the heat flux from the melt pool minus the power per unit area absorbed by the melting front, the heat flux into the ingot is essentially the same as the heat flux from the melt pool. As a result, the latent heat of melting absorbed due to the upwards ingot feed rate can be neglected.

To estimate the effect of the ingot's vertical feed rate on its temperature field consider the case of simple one-dimensional conduction in a moving medium governed by the fin equation:

$$\frac{d^2\theta}{dz^2} - M^2\theta - \frac{V}{\alpha}\frac{d\theta}{dx} = 0$$

$$\text{where } M^2 = \frac{hP}{kA},\ \theta = T - T_{ref}$$

and where T is temperature, T_{ref} is the temperature of the surroundings, z is the axial coordinate, h is the heat transfer coefficient, P is perimeter, k is thermal conductivity, A is cross-sectional area, V is the medium's velocity, and α is thermal diffusivity. Using the properties in Appendix A, an ingot radius of 2.54 cm, and choosing θ to be ~1000 K, we calculate $M^2\theta$ to be ~10^6. Referring again to Appendix A and choosing V, ΔT, and ΔZ as before, we calculate the

third term of the fin equation to be ~10^5. Thus the motion of the ingot can be neglected when calculating the temperature field within it.

Finally, an order of magnitude analysis shows that the melt pool axial velocities are at least ~10^{-3} m/s. This analysis is provided in Appendix B. Since the ingot feed rate is only ~10^{-5} m/s, the feed rate's effect upon the melt pool's velocities can be neglected.

Heat Flux at Melt Pool's Free Surface

While the above arguments allow for the neglecting of the ingot's motion, the mass flux from the melt pool's free surface still carries a sizable amount of sensible heat with it. This heat flux shall not be neglected in this analysis. Rather it shall be included in a computation of the net heat flux on the pool's free surface. This net heat flux will become the energy equation's boundary condition on the melt pool surface.

The net heat flux passing through the melt pool's free surface is calculated from four terms: heat flux from the electron beam, heat flux due to radiation, energy consumed during the evaporation process, and heat flux due to the loss of sensible heat carried out with the vapor. As mentioned above, the heat flux due to the electron beam as delivered by the actual system under study shall be modeled as a uniform heat flux across the pool surface. This flux is calculated according to the following expression:

$$q_{beam} = F_{pattern} F_{scatter} \frac{P}{\pi R^2}$$

where q_{beam} is the heat flux due to the electron beam, P is the power to the electron beam gun, and R is the ingot radius. The actual beam scan pattern causes a large portion of the beam power to go directly into the top of the crucible. $F_{pattern}$ is the percentage of the beam power that is directed at the ingot. Additionally, some of the electrons incident upon the ingot are scattered back without transferring their energy to it. $F_{scatter}$ is the percentage of electrons that do transfer their energy to the ingot.

Additional studies will be conducted that determine the system's response to alternate beam scanning patterns. This thesis shall consider patterns that provide Gaussian heat flux distributions. These beam heat flux distributions are calculated according to the following expression:

$$q_{beam}(r) = \frac{F_{pattern} F_{scatter} P}{2\pi\sigma^2\left(1 - e^{\frac{-R^2}{2\sigma^2}}\right)} e^{\frac{-r^2}{2\sigma^2}}$$

where σ is the gaussian distribution's standard deviation and r is radial position. This expression provides countless heat flux distributions that provide the same net [total] heat transfer to the ingot as the uniform heat flux distribution given above. This allows the effects of beam power's distribution to be studied separately from the effects of the total beam power delivered to the ingot.

The heat flux due to radiation is calculated assuming that the melt pool is surrounded by a nearly black environment consisting of a nonparticipating medium. This is an appropriate assumption since the coating chamber's walls and the hardware being coated are at much lower temperatures than the melt pool. The over-source heater may emit a sizable quantity of radiation but would be shielded by the hardware being coated. Since the deposition chamber is evacuated to promote evaporation of the TBC material, the environment should behave as a nonparticipating medium. Thus, the expression to calculate radiation from the melt pool's free surface is simply:

$$q_{rad} = \varepsilon\sigma_o T^4$$

where q_{rad} is the heat flux due to radiation, ε is Zirconia's emissivity, σ_o is Stefan-Boltzman constant, and T is temperature.

The calculation of the heat fluxes due to evaporation and the loss of sensible heat both require the computation of mass (or mole) flux from the melt pool's free surface. This is calculated using Langmuir's equation which governs the ideal rate of evaporation into a vacuum. This equation states:

$$J = \frac{p_v}{\sqrt{2\pi MR_u T}}$$

where J is the mole flux of the evaporating species, p_v is its vapor pressure, M is its molar mass, T is the absolute temperature, and R_u is the universal gas constant. The heat flux due the evaporation of Zirconia from the melt pool's free surface is then calculated according to the expression:

$$q_{evap} = h_{lv} MJ$$

where h_{lv} is the latent heat of vaporization of the evaporating species and M is its molecular mass. Similarly, the heat flux due to the loss of sensible heat carried off with the vapor is calculated according to:

$$q_{sens} = c_p TMJ$$

where c_p is the specific heat of the evaporating species, M is its molecular mass, and T is the absolute temperature.

Heat Flux between Melt Pool/Ingot and Crucible

As mentioned above, heat transfer between the ingot/melt pool and the crucible shall be modeled as convective with a single heat transfer coefficient. Thus, the equation governing this heat transfer is:

$$q = h_c\left(T - T_{ref}\right)$$

where q is the net heat flux between the melt pool or ingot and the crucible, h_c is the heat transfer coefficient, T is the absolute temperature of the ingot or melt pool, and T_{ref} is an ambient reference temperature associated with the crucible.

Due to a lack of information regarding the crucible and its internal cooling circuit, this heat transfer coefficient has been assigned an arbitrary value of 100 W/m ^{2}K. This order of magnitude estimate was provided by sources at the Lawrence Livermore National Laboratory working in the field of YSZ PVD. As part of this study, a sensitivity analysis shall be performed to assess the error introduced by the uncertainty in this value.

Because the crucible is water cooled, the reference temperature has been chosen as the boiling temperature of water, 373 K. And since the cooling water in the crucible should never approach its boiling point, this particular assumption underestimates the amount of heat transferred to the crucible; however, since the melting point of YSZ is 2988K the error introduced should be minimal.

Ingot "Bottom"

The entire ingot is not being modeled in this analysis. Only the upper portion of the ingot is included in the system being studied. By modeling only a portion of the entire ingot, more computational time can be devoted to the melt pool where the interesting behavior is occurring. However, we must now consider the boundary conditions that will be applied along the "cut" we make in the ingot when separating the top half for our analysis.

Recall from the argument to neglect the ingot motion, that the heat flux through the melting front is ~10^5 W/m^2. Assuming 1D conduction occurs throughout the remainder of the ingot (no heat flux to crucible occurs), a quick order of magnitude calculation can be performed to determine the length of ingot that must be considered before the temperature drops to, say, 373 K (the reference temperature used above):

$$q \sim k \frac{\Delta T_z}{\Delta z}$$

$$\Delta z \sim k \frac{\Delta T_z}{q} \sim 1\text{cm}$$

which is the order of magnitude of the ingot's radius.

Note that this analysis underestimates the value of Δz since the amount of heat conducted axially through the ingot decreases with depth. Nevertheless, it should be sufficient to model a portion of the ingot whose aspect ratio, r/h, is 1/3. In this ratio r is the ingot's radius and h is the length of the portion of the ingot being modeled in this system. Along the bottom edge of our computational domain we shall then model the ingot as isothermal at 373K.

Melt Pool Velocity and Stress Boundary Conditions

Having discussed all the features of the system related to the energy equation, attention shall now be turned towards those affecting the momentum equation. The only boundary involving any sort of complexity is the melt pool's free surface. Here variations in surface tension create stress, called Marangoni stress, which drags fluid along the pool's surface. This stress is governed by the equation:

$$\tau = \frac{\partial \sigma}{\partial T} \frac{\partial T}{\partial r}$$

where τ is the Maragoni stress, $d\sigma/dT$ is the local surface tension gradient, and dT/dr is the local temperature gradient. As mentioned in Appendix A, the surface tension gradient shall be modeled as a constant over all temperatures. It should also be noted that the melt pool's free surface shall be modeled as perfectly flat and rigid. The remaining melt pool boundaries consist of the crucible wall and the melting front. Along both of these boundaries the no-slip condition shall be assumed.

Thermophysical Properties

As mentioned in the introduction, a complete discussion of the thermophysical properties of YSZ can be found in Appendix A. Also recall that the actual melt pool contains the liquid phases of both Zirconia and Yttria. For this analysis, the presence of Yttria in the melt pool shall be neglected; therefore, the only liquid phase properties of interest are those of pure Zirconia. In addition, the properties of solid YSZ and molten Zirconia shall be assumed to be independent of temperature and pressure. The only exception is that the vapor pressure of liquid Zirconia, used in the computation of evaporative mass flux from the melt pool's surface, will retain its temperature dependence. A final assumption is that the solid ingot is not porous and has the same density as the melt pool. This assumption should not affect the results of our steady-state analysis.

Surface Tension Driven Flow versus Buoyancy Driven Flow

There are essentially two potential driving forces for fluid motion in the melt pool. The first is the shear stress generated on the melt pool's surface due to variations in surface tension with temperature. The second is the variation in density with temperature inside the melt pool. These driving forces couple together the Navier-Stokes and Energy Equations (discussed below) in such a manner that makes their solution rather difficult. If either of these driving forces could be shown to be negligible with respect to the other, our model of the melt pool would be made significantly simpler. An order of magnitude analysis is undertaken in Appendix B to analyze the relative importance of these two driving forces. Unfortunately, this analysis demonstrates that neither of these driving forces eclipses the other; therefore, both must be included in our model.

Finite Element Model & Summary

The modeling assumptions discussed above were eventually used to create a finite element model of the melt pool and ingot. Using this model, the governing equations of mass, momentum, and energy could be solved for the melt pool/ingot system. Written in terms of a cylindrical coordinate system, these equations are summarized as follows:

conservation of mass

$$\frac{1}{r}\frac{\partial}{\partial r}(ru_r)+\frac{\partial u_z}{\partial z}=0$$

the Navier-Stokes equations

$$\rho_o\left[\frac{\partial u_r}{\partial t}+u_r\frac{\partial u_r}{\partial r}+u_z\frac{\partial u_r}{\partial z}\right]=-\frac{\partial p}{\partial r}+\left[\frac{1}{r}\frac{\partial}{\partial r}\left(\mu r\frac{\partial u_r}{\partial r}\right)-\mu\frac{u_r}{r^2}+\frac{\partial}{\partial z}\left(\mu\frac{\partial u_r}{\partial z}\right)\right]+(\rho-\rho_o)g_r$$

$$\rho_o\left[\frac{\partial u_z}{\partial t}+u_r\frac{\partial u_z}{\partial r}+u_z\frac{\partial u_z}{\partial z}\right]=-\frac{\partial p}{\partial z}+\left[\frac{1}{r}\frac{\partial}{\partial r}\left(\mu r\frac{\partial u_z}{\partial r}\right)+\frac{\partial}{\partial z}\left(\mu\frac{\partial u_z}{\partial z}\right)\right]+(\rho-\rho_o)g_z$$

and the energy equation.

$$\rho_o c_p\left[\frac{\partial T^L}{\partial t}+u_r\frac{\partial T^L}{\partial r}+u_z\frac{\partial T^L}{\partial z}\right]=\left[\frac{1}{r}\frac{\partial}{\partial r}\left(kr\frac{\partial T^L}{\partial r}\right)+\frac{\partial}{\partial z}\left(k\frac{\partial T^L}{\partial z}\right)\right]+\Phi$$

where the variables used can be found in the notation summary at the start of this thesis. This set of four equations contains five unknowns, namely: u_z, u_r, T, ρ, and p. To solve this system a fifth equation is required. For this purpose, the equation of state for the Boussinesq Approximation shall be employed:

$$\rho-\rho_o=-\rho_o\left[\beta_T(T^L-T^L{}_o)+\sum_n\beta_n c_n\right]$$

By substituting this expression into the Navier-Stokes equations, ρ is eliminated and a system of four equations and four unknowns is obtained. Note that the melt pool is being modeled with only a single species so the second term in the brackets can be dropped.

These equations are solved in a discretized fashion on a fixed mesh. This mesh provides a computational domain representative of the melt pool and ingot. To create the effect of two distinct phases of matter, a variable property approach has been taken. In this approach, the thermophysical properties at any point in the mesh are determined by the local temperature. At locations below the melting point, the properties are those of solid YSZ. At locations above the melting point, the properties are those of molten Zirconia. Viscosity takes on some large value below the melting point in order to eliminate relative motion within the solid phase. To prevent computational difficulties, the properties are ramped between their solid and liquid values across a small temperature range centered around the melting point.

In addition, enthalpy data are entered rather than specific heat data. Then specific heat is calculated according to its thermodynamic definition:

$$c_p=\left.\frac{\partial h}{\partial T}\right|_p$$

where c_p is specific heat, h is enthalpy, and T is absolute temperature. Even though its effects are small, the latent heat of melting is created by ramping enthalpy over an amount equal to the latent heat across the small temperature range mentioned above.

Most of the boundary conditions being applied to the finite element model have been described in detail earlier in this chapter. They are repeated here simply to provide a concise summary of the entire model. In addition, the following paragraphs shall address the remaining boundary conditions which have yet to be discussed.

On the melt pool's free surface velocity in the axial direction is zero and radial stresses are imposed by surface tension gradients. There also exists a heat flux due to the electron beam, radiation, evaporation, and the loss of sensible heat:

$$u_z = 0$$

$$\mu \frac{\partial u_r}{\partial r} = \frac{\partial \sigma}{\partial T^L} \frac{\partial T^L}{\partial r}$$

$$q = -k \frac{\partial T^L}{\partial z} = B(r) - \varepsilon \sigma {}_o T^4 - \frac{h_{lv} M p_v}{\sqrt{2\pi MRT^L}} - \frac{c_p T M p_v}{\sqrt{2\pi MRT^L}}$$

On the melt pool's sides both axial and radial velocities are zero and there exists heat flux into the crucible. This heat flux is modeled as purely convective with a constant heat transfer coefficient and reference temperature:

$$u_r = u_z = 0$$

$$q = -k \frac{\partial T^L}{\partial r} = h_c \left(T^L - T_{ref} \right)$$

On the melt pool's bottom surface conservation of mass between the ingot and the melt pool is observed. A no slip condition is enforced inside the melt pool along this melting front. And, the temperatures of the ingot and melt pool along this surface are equal to the melting point of YSZ:

$$\rho^S \left[n_r \left(u_r{}^S - u_r{}^* \right) + n_z \left(u_z{}^S - u_z{}^* \right) \right] = \rho^L \left[n_r \left(u_r{}^L - u_r{}^* \right) + n_z \left(u_z{}^L - u_z{}^* \right) \right]$$

$$n_r \left(u_z{}^L - u_z{}^S \right) - n_z \left(u_r{}^L - u_r{}^S \right) = 0$$

$$T^L = T^S = T_{mp}$$

Note that the location of the pool's bottom surface is introduced as another unknown in this model. This fifth unknown requires a fifth equation. This

equation is derived from conservation of energy across the melting front which states that the net rate of heat flux into the melting front is equal to the rate of energy used per unit area in melting the ingot:

$$k^L\left(n_r\frac{\partial T^L}{\partial r}+n_z\frac{\partial T^L}{\partial z}\right)-k^S\left(n_r\frac{\partial T^S}{\partial r}+n_z\frac{\partial T^S}{\partial z}\right)=\rho^S h_{sl}\left[n_r\left(u_r{}^S-u_r{}^*\right)+n_z\left(u_z{}^S-u_z{}^*\right)\right]$$

The ingot is modeled as stationary; therefore, no motion occurs at any of the ingot boundaries. The sides of the ingot experience a convective heat transfer similar to the pool's sides. The bottom of the ingot is modeled as an isothermal surface at the reference temperature used in the convective heat transfer equations for the melt pool and ingot sides

$$q_{sides}=-k\frac{\partial T^S}{\partial r}=h_c\left(T^S-T_{ref}\right)$$

$$T_{bottom}=T_{ref}$$

As mentioned, the governing equations, thermophysical properties, and boundary conditions described above were applied to a finite element model of the system. A solution for the temperature and velocity fields was then obtained using the commercial fluid dynamics analysis package, FIDAP. Solutions were obtained through a standard Newton-Raphson iterative procedure.

Chapter 3.0 Dimensional Analysis

The analysis of the melt pool and ingot can be simplified by converting this system to an equivalent dimensionless system. To begin this process, it is first necessary to define the dependent and independent parameters of interest in this study. Then the Buckingham Pi Theorem can be applied and the parameters can be grouped into dimensionless quantities. Alternatively, by rewriting the governing equations in an appropriate dimensionless format, it becomes obvious how to replace the parameters of interest with their dimensionless counterparts during this analysis.

The dependent parameters being studied in this thesis should, in some way, represent the important features of the melt pool. Further, the features of the melt pool considered important are those that would somehow impact the quality of the TBC being manufactured through this process. During the deposition portion of the PVD process, there are many factors that can affect the quality of the TBC. For all intents and purposes, only three of these factors are related to conditions associated with the melt pool. These factors are: the rate of deposition of material on the hardware being coated, the temperature of the vapor flux as it approaches the hardware, and the temperature of the hardware being coated itself. Each of these factors can have an impact upon the microstructure of the final TBC. With these factors in mind, the important features of the melt pool can be selected.

The melt pool's impact upon each of the deposition factors mentioned above is solely through the temperature distribution across its surface. The deposition rate of material is related to the local evaporation of material from the pool's surface. This evaporation rate is a function of pool surface temperature only. The temperature of the vapor flux as it approaches the hardware being coated is obviously related to its temperature as it leaves the melt pool's surface. And, the temperature of the hardware being coated is influenced by, among other things, the heat transferred to it from the melt pool. This would be a function of the melt pool's surface temperature. Thus, a study of the temperature distribution across the melt pool's free surface would be sufficient in order to document its impact upon TBC fabrication by the PVD process.

Figure 3-1 attempts to illustrate the dependencies discussed above. It depicts a sampling of parameters that might be altered during the PVD process. The arrows show how variations in one parameter might affect other parameters. The parameters in this figure can influence any other parameter that they point to (the influence goes from left to right). For example, a variation in part geometry could affect the local deposition rate on the part which could in turn affect the quality of the TBC being manufactured on that part. This figure also shows that TBC quality could be affected in several ways by the melt pool temperature. This figure also shows, however, that TBC quality is influenced by

many other factors that shall not be considered in this thesis (and even by some I have not included in this figure).

Figure 3-1 Important Factors upon which TBC Quality Depends

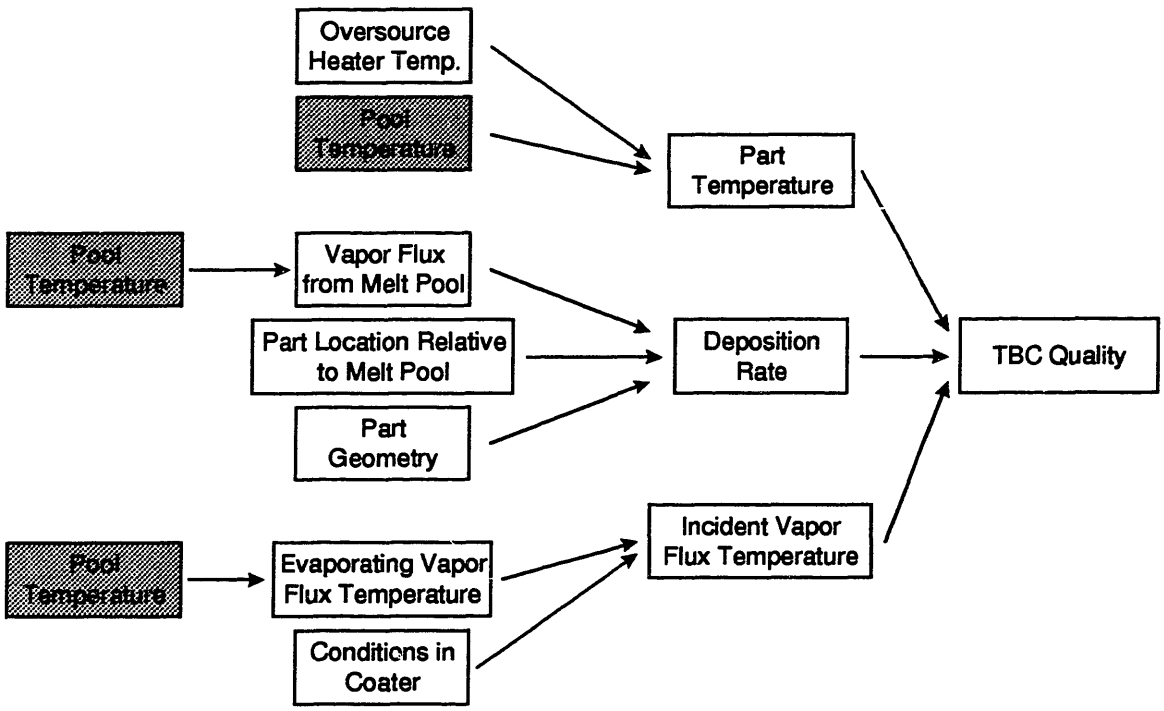

Although knowledge of the melt pool's surface temperature distribution would be sufficient in a study of the melt pool's influence upon the PVD process, it is necessary to study features of the melt pool that can be represented by simple scalar quantities. Data for these quantities are easier to display visually. More importantly, relations between these quantities and various independent parameters can also be formulated. An overall study of the PVD process could then determine the relations between these quantities and the final quality of the TBC. Finally, it might be possible to measure some of these quantities during an actual PVD process in order to aid in the control of the process.

Three scalar parameters have been selected for study in this thesis. The first is the average melt pool surface temperature, T_{avg}. The second is the total evaporation rate from the melt pool's surface, $\dot{m}$. The third is the difference between the maximum and minimum melt pool surface temperatures: ΔT_{surf}. T_{avg} helps to quantify the heat transfer from the pool's surface and the temperature of the vapor flux leaving the pool. $\dot{m}$ helps to quantify the vapor flow rate leaving the pool's surface. And, ΔT_{surf} helps to quantify the distribution of vapor flux and the vapor flux's temperature across the pool's surface. In terms of Figure 3-1, these three parameters are intended to capture each of the "routes" from pool

temperature to TBC quality. This completes the selection of the dependent parameters for study in this system.

As discussed, knowledge of the temperature distribution across the melt pool's surface is sufficient for a study of the entire PVD process. In fact, each of the three dependent parameters selected could be calculated from that distribution. Therefore, each of these three quantities should be dependent upon the same independent parameters that influence the melt pool's surface temperature distribution.

Through our knowledge of the melt pool/ingot system's governing equations and boundary conditions, the following relation could be proposed:

$$T_{surf}(r) = f\left(\rho, \mu, \beta, c_p, k, \frac{\partial \sigma}{\partial T}, g, h_c, L, q, \sigma, \varepsilon, p_v(T), M, h_{lv}, \rho^s, c_p{}^s, k^s\right)$$

where $T_{surf}(r)$ is the melt pool surface temperature,
- ρ is the melt pool density,
- μ is the melt pool viscosity,
- β is the melt pool volume expansion coefficient,
- c_p is the melt pool specific heat,
- k is the melt pool thermal conductivity,
- $d\sigma/dT$ is the surface tension coefficient (a constant gradient),
- g is gravity,
- h_c is the heat transfer coefficient between the ingot/melt pool and crucible,
- L is a length scale of the system,
- q is the average heat flux from the electron beam,
- σ is the standard deviation of the heat flux's [Gaussian] distribution,
- ε is the melt pool emissivity,
- $p_v(T)$ is the vapor pressure versus temperature relation for Zirconia,
- M is the molecular weight of Zirconia,
- h_{lv} is the latent heat of vaporization for Zirconia,
- ρ^s is the density of the solid ingot,
- $c_p{}^s$ is the specific heat of the solid ingot, and
- k^s is the thermal conductivity of the solid ingot.

Note that the radius of the ingot, R, shall be chosen to represent the length scale of the system, L.

Before beginning a dimensional analysis of the system, consideration should first be given to the relative importance of the independent parameters shown in the above relation. Most of the parameters in the above list, are thermophysical or physical properties of the melt pool or ingot. While it is true that all of these properties belong in the proposed relation, these quantities do not represent controllable parameters of the melt pool / ingot system. For example, it is

unlikely that a PVD manufacturer looking to alter the temperature distribution across the melt pool will directly alter, say, the thermal conductivity of the pool.

However, since the property data has some degree of uncertainty in it, it would be prudent to study their effect upon the temperature distribution on the pool's surface. Determining the pool's sensitivity to these properties will establish bounds on the error introduced by this uncertainty. We might, therefore, separate our parameters into two groups: one group which contains controllable parameters and a second group consisting of thermophysical properties which influence the surface temperature distribution but cannot be controlled:

$$T_{surf}(r) = f\left(\underbrace{h_c, L, q, \sigma}_{\text{Controllable Parameters}}, \underbrace{\rho, \mu, \beta, c_p, k, \frac{\partial \sigma}{\partial T}, g, \varepsilon, p_v(T), M, h_{lv}, h_{sl}\, \rho^s, c_p{}^s, k^s}_{\text{ThermophysicalProperties}} \right)$$

where it is fairly obvious that h_c, L, q, and σ are the only four parameters that might be easily controlled during TBC production.

In this thesis, we shall not study the effects of varying the thermophysical properties of the solid ingot, ρ^s, $c_p{}^s$, and k^s. These properties are known with more certainty than the liquid properties. In addition, their influence upon the pool surface temperature distribution should be less important than the influence of the melt pool's properties. As a consequence, the solid properties should introduce less error into the model than their liquid counterparts. Similarly, this thesis shall also neglect the uncertainty in the quantities used to compute the net heat flux through the pool's surface. These quantities include emissivity, vapor pressure, the latent heat of vaporization, and molecular weight. These quantities are also known with more certainty than the liquid properties.

Also note that while gravity is an influential parameter in this study, its only appearance in the governing equations and boundary equations occurs in the term βg. As a result, it is not necessary to study the effects of β and g separately. These two terms can be replaced by their product in the proposed relation. As a result of neglecting the mentioned parameters and combining these two terms, our relation simplifies to the following:

$$T_{surf}(r) = f\left(\underbrace{h_c, L, q, \sigma}_{\text{Controllable Parameters}}, \underbrace{\rho, \mu, \beta g, c_p, k, \frac{\partial \sigma}{\partial T}}_{\text{Thermophysical Properties}} \right)$$

Consequently, the following functional dependencies shall be proposed for each of the selected dependent parameters:

$$T_{avg} = f_1\left(\underbrace{h_c, L, q, \sigma}_{\text{Controllable Parameters}}, \underbrace{\rho, \mu, \beta g, c_p, k, \frac{\partial \sigma}{\partial T}}_{\text{Thermophysical Properties}} \right)$$

$$\dot{m}(r) = f_2\left(\underbrace{h_c, L, q, \sigma}_{\text{Controllable Parameters}}, \underbrace{\rho, \mu, \beta g, c_p, k, \frac{\partial \sigma}{\partial T}}_{\text{Thermophysical Properties}} \right)$$

$$\Delta T_{surf} = f_3\left(\underbrace{h_c, L, q, \sigma}_{\text{Controllable Parameters}}, \underbrace{\rho, \mu, \beta g, c_p, k, \frac{\partial \sigma}{\partial T}}_{\text{Thermophysical Properties}} \right)$$

Having now selected both the dependent and independent parameters for study in this thesis, they can be grouped into dimensionless quantities.

The first step in forming these dimensionless groups is selecting a set of primary dimensions. This study shall use a set of five primary dimensions: length, time, mass, temperature, and power. Note that an important assumption regarding the character of the melt pool is implied in choosing a set of five primary dimensions. This is because power is equal to force times velocity, and both of these quantities can be written in terms of the other four primary dimensions. Selecting power as an independent primary dimension is equivalent to neglecting the fact that kinetic energy can be converted to thermal energy. In fluid flow this process would be observed as kinetic energy is converted into thermal energy through viscous dissipation. In essence, selecting power as a fifth primary dimension is equivalent to neglecting viscous dissipation. This assumption is fine as long as we are considering a low-speed flow phenomenon. In the case of motion within the melt pool, this assumption should be quite valid.

The next step is to select five parameters for use in nondimensionalizing the remaining parameters. The five parameters selected for this purpose are: k, ρ, μ, L, and ΔT. The first four parameters are four of the independent quantities in the above relations: thermal conductivity, density, viscosity, and ingot radius. The final parameter, ΔT, is an arbitrary temperature difference selected for convenience. Recall from our arguments to neglect the ingot feed rate in

Chapter 2.0 that the temperature difference between the pool surface and ingot is expected to be of the order of 100K. Therefore, if we assign to ΔT a value of 100K, our calculated dimensionless temperature differences between the pool surface and the melting front should be of order unity.

The proposed functions for each of our selected dependent quantities each contain a total of 10 independent parameters between their two parts (the controllable part and the error part). Since ΔT effectively adds another parameter to the list of independent parameters, there are now a total of 11 independent parameters. The Buckingham Pi Theorem states that these parameters can be grouped into 11-5=6 dimensionless independent quantities in addition to each of the three dependent dimensionless quantities. Using k, ρ, μ, L, and ΔT to form these groups, the following functional dependencies are obtained:

$$\theta_{avg} = f_1 * \left(Nu_q, Nu_{hc}, \sigma^*, Gr, \Pr, St\right)$$
$$\dot{m}^* = f_2 * \left(Nu_q, Nu_{hc}, \sigma^*, Gr, \Pr, St\right)$$
$$\Delta\theta_{surf} = f_3 * \left(Nu_q, Nu_{hc}, \sigma^*, Gr, \Pr, St\right)$$

where:

θ is a dimensionless temperature defined by $\frac{T - T_{ref}}{\Delta T}$,

$\dot{m}^*$ is a dimensionless vapor flow rate defined by $\frac{\dot{m}}{\mu L}$,

Gr is the Grashof Number defined by $\frac{\beta \Delta T g L^3 \rho^2}{\mu^2}$,

Pr is the Prandtl Number defined by $\frac{c_p \mu}{k}$,

St is a dimensionless surface tension gradient defined by $\frac{\Delta T \rho L}{\mu^2}\frac{\partial \sigma}{\partial T}$,

Nu_q is the Nusselt Number based on q defined by $\frac{qL}{k\Delta T}$,

Nu_{hc} is the Nusselt Number based on h_c defined by $\frac{h_c L}{k}$,

and σ^* is a dimensionless standard deviation for the electron beam's heat flux defined by $\frac{\sigma}{L}$,

As seen, grouping all the parameters as such has reduced the number of independent variables that must be studied to only six. This greatly reduces the

number of computations needed to map the relationships between the dependent and independent parameters.

These groupings can be formed in an alternative manner by multiplying the governing equations and boundary conditions by appropriate combinations of the selected independent parameters (k, ρ, μ, L, and ΔT). The dimensionless groups formed above will then take the place of their dimensioned counterparts. This method will, of course, produce dimensionless groups for all variables rather than just those of particular interest. Starting with the Navier-Stokes equations, this process would go as follows:

$$\left[\frac{\partial u_i}{\partial t}+u_j\frac{\partial}{\partial x_j}=-\frac{1}{\rho_o}\frac{\partial p}{\partial x_j}+\frac{\mu}{\rho_o}\frac{\partial^2 u_j}{\partial x_j^2}+\beta(T-T_o)ge_i\right]\times\frac{L^3\rho^2}{\mu^2}$$

$$\frac{\partial\left(\frac{\rho L u_i}{\mu}\right)}{\partial\left(\frac{t\mu}{\rho L^2}\right)}+\left(\frac{\rho L u_j}{\mu}\right)\frac{\partial\left(\frac{\rho L u_i}{\mu}\right)}{\partial\left(\frac{x_j}{L}\right)}=-\frac{\partial\left(\frac{pL^2\rho}{\mu^2}\right)}{\partial\left(\frac{x_j}{L}\right)}+\frac{\partial^2\left(\frac{\rho L u_j}{\mu}\right)}{\partial\left(\frac{x_j}{L}\right)^2}+\frac{\beta g\Delta T L^3\rho^2}{\mu^2}\frac{T-T_o}{\Delta T}e_i$$

$$\frac{\partial u_i^*}{\partial t^*}+u_j^*\frac{\partial u_i^*}{\partial x_j^*}=-\frac{\partial p^*}{\partial x_j^*}+\frac{\partial^2 u_j^*}{\partial x_j^{*2}}+Gr(T^*-T_o^*)e_i$$

Conversion of this equation to the above dimensionless form implies dimensionless forms for velocity $\left(\frac{\rho Lu}{\mu}\right)$, time $\left(\frac{t\mu}{\rho L^2}\right)$, position $\left(\frac{x}{L}\right)$, pressure $\left(\frac{pL^2\rho}{\mu^2}\right)$, volume expansion times gravity $\left(\frac{\beta g\Delta T L^3\rho^2}{\mu^2}\right)$, and temperature $\left(\frac{T-T_{ref}}{\Delta T}\right)$. Also implied is that the dimensionless quantities for both density and viscosity are unity. Of course, this nondimensionalization has been performed in such a manner as to agree with the previous method. Note that velocity's dimensionless group is Reynold's number.

This process could be continued by next considering the energy equation:

$$\left[\rho c_p\left(\frac{\partial T}{\partial t}+u_j\frac{\partial T}{\partial x_j}\right)=\mu\left(\frac{\partial u_i}{\partial x_j}+\frac{\partial u_j}{\partial x_i}\right)\frac{\partial u_i}{\partial x_j}+k\frac{\partial^2 T}{\partial x_j^2}\right]\times\frac{L^2}{k\Delta T}$$

$$\frac{\rho}{\rho}\frac{c_p\mu}{k}\left(\frac{\partial\left(\frac{T-T_{ref}}{\Delta T}\right)}{\partial\left(\frac{t\mu}{\rho L^2}\right)}+\frac{\rho u_j L}{\mu}\frac{\partial\left(\frac{T-T_{ref}}{\Delta T}\right)}{\partial\left(\frac{x_j}{L}\right)}\right)=\frac{\mu^3}{\rho^2L^2k\Delta T}\left(\frac{\partial\left(\frac{\rho u_i L}{\mu}\right)}{\partial\left(\frac{x_j}{L}\right)}+\frac{\partial\left(\frac{\rho u_j L}{\mu}\right)}{\partial\left(\frac{x_i}{L}\right)}\right)\frac{\partial\left(\frac{\rho u_i L}{\mu}\right)}{\partial\left(\frac{x_j}{L}\right)}+\frac{k}{k}\frac{\partial^2\left(\frac{T-T_{ref}}{\Delta T}\right)}{\partial\left(\frac{x_j}{L}\right)^2}$$

Note that the second term of the energy equation represents viscous dissipation, an effect that was neglected by selecting five primary dimensions during the first method of nondimensionalization. In this method, note that the second term suggests a second dimensionless form for viscosity. This operation nondimensionalizes a kinetic term, μ, using the thermal parameters k and ΔT. Recall that the assumption made during the first method was that thermal and kinetic energies were not interchangeable. To stay consistent in our assumptions, the viscous dissipation term will be neglected and the first dimensionless form for viscosity (unity) shall be used. This method, however, does help support this assumption since the dimensionless form of viscosity found in the viscous dissipation term above is ~10^{-9}. Since the coefficients in front of the other two terms are much larger, it should be safe to neglect the viscous dissipation term and its effects. Returning to the dimensionless form of the energy equation written above, it is implied that specific heat would be nondimensionalized as $\frac{c_p\mu}{k}$ while thermal conductivity would become unity in dimensionless form.

The remaining parameters would be nondimensionalized through various boundary conditions of the melt pool/ingot system and some phenomenological laws. These operations would appear as follows:

$$\left[\tau=\frac{\partial\sigma}{\partial T}\frac{\partial T}{\partial x_r}=\mu\frac{\partial u_r}{\partial z}\right]\times\frac{\rho L^2}{\mu^2}$$

$$\left(\frac{\Delta T\rho L}{\mu^2}\frac{\partial\sigma}{\partial T}\right)\frac{\partial\left(\frac{T-T_{ref}}{\Delta T}\right)}{\partial\left(\frac{x_r}{L}\right)}=\frac{\partial\left(\frac{\rho u_r L}{\mu}\right)}{\partial\left(\frac{z}{L}\right)}$$

where the dimensionless form of the surface tension gradient is $\frac{\Delta T\rho L}{\mu^2}\frac{\partial\sigma}{\partial T}$,

$$\left[q = k\frac{\partial T}{\partial x}\right] \times \frac{L}{k\Delta T}$$

$$\frac{qL}{k\Delta T} = \frac{\partial\left(\frac{T - Tref}{\Delta T}\right)}{\partial\left(\frac{x}{L}\right)}$$

where the dimensionless form of heat transfer is $\frac{qL}{k\Delta T}$.

$$q = h_c(T - T_r) \times \frac{L}{k\Delta T}$$

$$\frac{qL}{k\Delta T} = \frac{h_c L}{K}\left(\frac{T - T_r}{\Delta T}\right)$$

where the dimensionless form of the heat transfer coefficient is $\frac{h_c L}{K}$, and

$$\left[q = h_{sl}\mu\right] \times \frac{L}{k\Delta T}$$

$$\frac{qL}{k\Delta T} = \frac{h_{sl}\mu}{k\Delta T}\frac{\rho L u}{\mu}$$

where the dimensionless form of the latent heat of melting is $\frac{h_{sl}\mu}{k\Delta T}$.

This method of nondimensionalizing the melt pool/ingot system is quite complete and a bit more mathematically rigid than the first method. However, the first method is invaluable since it provides succinct proposals for the functional dependencies of each dependent parameter being studied.

Chapter 4.0 Experimental Simulations

The previous chapter laid much of the groundwork for the experimental portion of this thesis. Recall that our interest lies solely in the temperature and vapor flux distributions on the melt pool's surface. Also recall that three independent parameters have been selected to characterize these distributions: T_{avg}, $\dot{m}$, and ΔT_{surf}. Through the work carried out in the previous chapter, it has also been decided that the dimensionless forms of these parameters, θ_{avg}, $\dot{m}^*$, and $\Delta\theta_{surf}$, shall depend upon only six independent dimensionless parameters: Gr, Pr, St, Nu_q, Nu_{hc}, and σ^*. The first three parameters, Gr, Pr, and St, represent thermophysical properties of the melt pool. These parameters are included in the study to determine the bounds upon the error introduced by uncertainty in the properties. The other three parameters represent controllable features of the melt pool during the fabrication of TBCs.

With these developments in mind, a series of experimental simulations was planned in order to map the dependencies of the dependent parameters upon each of the independent parameters. Each of the simulations would begin with a steady-state solution of the melt pool/ingot system. This solution would be obtained using values for all of the independent parameters that best approximate the actual operating conditions of the PVD system being studied in this thesis. Table 4-1 contains values for all the parameters used in the computation of this starting point solution. Each simulation would then vary one of the independent dimensionless parameters and record the melt pool's response. The parameters would typically be varied in two directions (made both larger and smaller) over a series of finite steps.

Many of the properties that comprise the parameters Gr, Pr, and St, were estimated by order of magnitude approximations. Since these parameters were being used to establish error due to property uncertainty, they were each varied over two orders of magnitude in twenty finite steps. For example, at the starting-point solution, Pr has a value of 21.8. Pr was varied down to a value of 2.18 in ten steps and up to a value of 218 in another ten steps. While the Pr is comprised of three properties and could, in the worst case, be off by three orders of magnitude, this situation is highly unlikely. It is more likely that the Pr number is correct to at least a single order of magnitude; therefore, the planned experiment should be more than sufficient. The same is true for Gr and St.

The remaining three parameters, Nu_q, Nu_{hc} and σ^*, represent controllable parameters and should be varied over corresponding realistic ranges. The experimental simulation that varies Nu_q is essentially an experiment to investigate the effects of varying the average heat flux due to the electron beam. Note that the starting-point solution uses a uniform distribution of beam heat flux. Therefore, in this simulation the distribution of the beam flux shall remain

uniform. The range over which the magnitude of Nu_q was varied was determined by considering the range over which the beam power could be possibly varied. The starting point value corresponds to a beam power of 50kW. While the electron beam gun currently in use has a maximum power rating of 60kW, it is plausible that a more powerful gun could be put into service. Therefore, the range over which q might vary has been arbitrarily to lie between 25kW (half of the starting value) and 100kW (twice the starting value). Thus, Nu_q was varied between 460 and 1840 using a uniform distribution of heat flux. Nu_q was varied over 20 finite steps.

Table 4-1 Parameters used in the Starting Point Solution of the Melt Pool/Ingot System

Independent Parameters Under Investigation:	
Gr	1.27E5
Pr	21.8
St	2.67E3
Nu_q	919
Nu_{hc}	0.94
σ^*	Infinite (Uniform Distribution from Beam)
Independent Parameters Not Under Investigation:	
ρ^{s*}	1
k^{s*}	0.37
$c_p{}^{s*}$	15.6
$h_{sl}{}^*$	109.9

Note: h_{lv}, M, $p_v(T)$, and ε were never converted to dimensionless quantities. They were used instead to calculate the net heat flux into the pool's surface which itself was converted into a dimensionless number & used in the numerical simulations.

The experiments which examine the effect of varying σ^* are essentially aimed at examining the effects of varying the distribution of heat flux provided by the electron beam. Recall from Chapter 2 that Gaussian distributions shall only be considered in this regard. Also recall that the formula being used to calculate these distributions assures the ingot always receives the same net heat transfer regardless of the distribution's standard deviation, σ. This makes it easier to vary σ^* while holding Nu_q constant during this experimental simulation.

The range over which σ^* shall be varied has been chosen to lie between 2.0 and 0.25. Figure 4-1 shows the beam's heat flux distributions at the extreme values of σ^* for this experiment. Note that when σ^* is equal to 2.0 the Gaussian heat flux distribution is nearly indiscernible from the uniform distribution. As σ^* is

decreased, more of the electron beam's energy is concentrated in the center of the ingot. The numerical simulations showed that when s* neared a value of 0.25, the edges of the ingot began to solidify. Since this steady-state scenario would be useless in a commercial PVD system, there is no point in examining values of σ^* any smaller than this. This dimensionless parameter was varied between 2.0 and 0.25 over 10 finite steps.

The experiments which examine the effect of varying Nu_{hc} are aimed at examining the effects of varying the heat transfer coefficient between the ingot/melt pool and the crucible. The heat transfer coefficient used at the starting point was chosen to have a value of 100 W/ mK producing a value of 0.94 for Nu_{hc}. This value is an estimate that is representative of measurements taken from systems similar to ours. This dimensionless parameter was varied over two orders of magnitude covering the range between 0.094 and 9.4. The experiment was carried out over 20 finite steps.

Figure 4-1
Nusselt Number based on Heat Flux due to Electron Beam
versus Dimensionless Radial Cooridinate

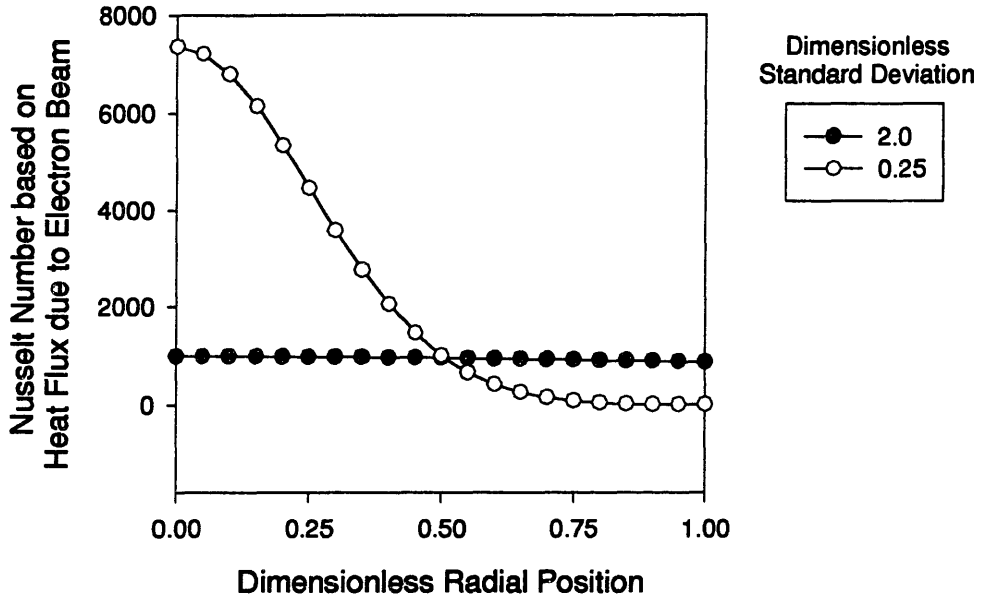

Table 4-2 summarizes all the experimental simulations being performed and reported in this thesis. It lists the range over which each parameter was varied and the number of finite steps taken to cover this range. Once these simulations were performed, the solutions generated for the melt pool and ingot system were then analyzed. Of course, the dependent quantities ΔT_{surf}, $\dot{m}$, and T_{avg} were calculated for each solution. In addition, the melt pool's velocity and

temperature fields were checked to see if they could be characterized by different regimes (e.g. different numbers of flow loops, different pool shapes, etc.). Finally, expressions relating our independent and dependent parameters were postulated and proposed.

Table 4-2 Summary of Experiments

Dimensionless Variable	Range of Variable during Experiment	Steps
Pr	2.18 - 218	20
Gr	1.27E4 - 1.27E6	20
St	2.67E2 - 2.67E4	20
Nu_q	460 - 1840	20
Nu_{hc}	.094 - 9.4	20
σ^*	0.25 - 2.0	10

Chapter 5.0 Results and Discussion

After the numerical experiments discussed in the previous chapter were performed, the data that had been generated was reviewed and analyzed. Each of the solutions generated was first checked for numerical convergence. Then, analysis of the results was begun with a visual examination. During this process, general trends could be observed in the velocity and temperature fields. In addition, transitions between several different regimes could be observed. Then the solutions were more closely analyzed by extracting the three independent parameters being studied. A quantitative error analysis was performed using the three experiments devoted to uncertainty in the thermophysical properties. The data was normalized with respect to the starting point data, plotted, and fit to curves. The curve fits were then combined to produce a general function relating each of the dependent parameters to each of the independent, controllable parameters.

Owing to the fact that our finite element analysis relies upon iterative methods, it is possible in certain instances for these techniques to fail to find a plausible solution which satisfies the our governing equations and boundary conditions. There are two reasons for such a failure. First, the problem we are attempting to solve could be ill-posed. In this case, a solution to our problem does not exist to be found. Second, the numerical methods we are employing may simply be unable to converge upon the solution we are seeking. We are all, no doubt, familiar with examples were Newton's method is unable to converge upon the root of a function, f(x)=0, given certain initial iterates. [1] A similar situation is possible when employing finite element techniques.

The problem we are attempting to solve in this thesis did, in fact, show a great deal of sensitivity to the initial iterate that we provided. In fact, our starting-point solution had to be obtained by building a finite element model in several steps. The initial model was quite basic and included only a few features of our system. Each successive step incorporated more features of the system and used the solution from the previous step as its initial iterate. These initial iterates provided our iterative techniques with solutions that were reasonably close to the ones they were seeking and aided in their convergence.

Similarly, our numerical experiments varied the independent parameters we were studying in small, finite steps. Each step used the solution from the previous step as an initial iterate. As a result of our finite element model's demonstrated sensitivity to the initial iterate provided to it, it is likely that making a "large" change to any of the independent parameters would prevent our finite element techniques from converging upon a new solution. Therefore, it was critical to use enough steps in each of our numerical simulations so that each step changed the independent parameter being studied by a sufficiently small amount.

Another difficulty faced in trying to obtain a converged solution from a finite element model, is that of designing a proper mesh. If the mesh we provide is not fine enough (does not contain a sufficient number of nodes), then it may not be able to capture the finer details of the solution being sought. This can cause our iterative techniques to converge slowly or fail to converge altogether.

This being said, the solutions generated during each step of each experimental simulation were checked for numerical convergence before any analysis was begun. The simulations where the Prandtl number was set to 218, 2.74, and 2.18 all did not converge successfully upon solutions. These experiments lay at the extreme high and low portions of the Prandtl number range being examined. Their results were discarded effectively narrowing the range over which the Prandtl number's effect was examined. In addition, each of the last four (out of ten) steps of the σ^* experiment did not converge. Since these four steps represented a significant portion of this experiment, extra time was spent in order to obtain results at these steps. First, new meshes were designed in order to provide more nodes in locations where small scales of activity were anticipated. Second, for each of these steps models were built in stages in a manner similar to that used to build the starting-point model. This added effort was rewarded and converged solutions were eventually obtained at each of these steps. All of the remaining steps in each of the other experiments converged upon realistic solutions.

Next, a visual analysis of the experimental data was undertaken. The information gathered from this qualitative analysis could be used to better understand the behavior of the melt pool. This understanding helps to explain the quantitative results compiled later. The visual analysis of the system was started by first examining its behavior using the starting point operating parameters. Figures 5-1 through 5-4 display various aspects of the melt pool under these conditions. These plots show the temperature field within the melt pool and ingot, the temperature field within the melt pool only, the velocity field within the melt pool, and the temperature distribution across the melt pool's surface, respectively. Note that each of the figures shows only half of the system since it is being modeled as axisymmetric. In addition, Figure 5-1 shows the ingot and melt pool system lying on its side (r^* pointing up) while Figures 5-2 and 5-3 show the system upright (r^* pointing left). And finally, in Figure 5-4, r^* is measured from the centerline to the edge of the melt pool.

Figure 5-1 is included to provide an overall impression of the temperature distribution throughout the entire system under standard operating conditions. The dimensionless temperature quantity has been defined so as to make the dimensionless melting temperature zero. All positive temperatures correspond

Figure 5-1 Dimensionless Temperature Field within the Melt Pool and Ingot Under Standard Operating Conditions

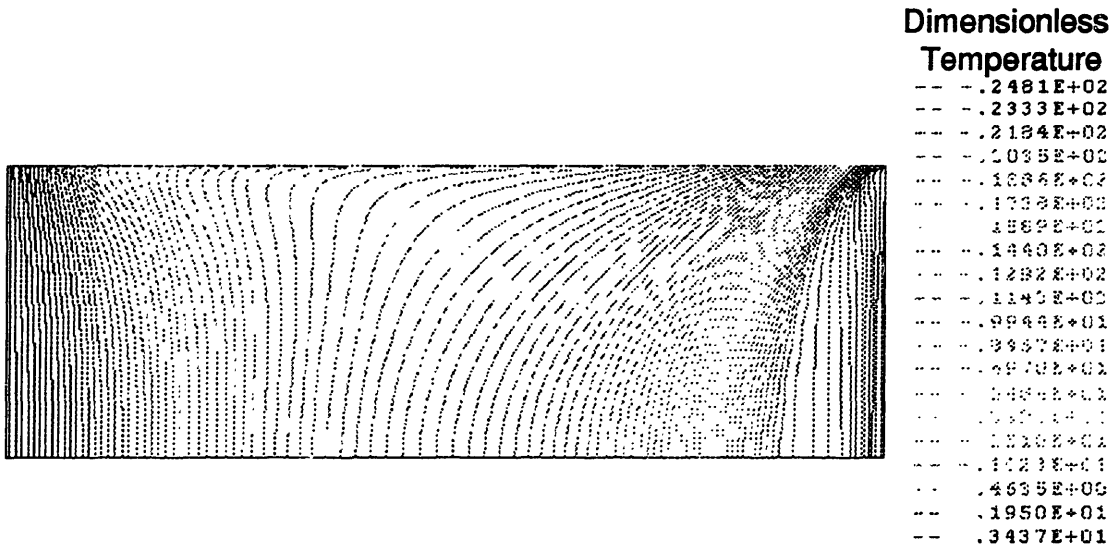

Figure 5-2 Dimensionless Temperature Field within the Melt Pool Under Standard Operating Conditions

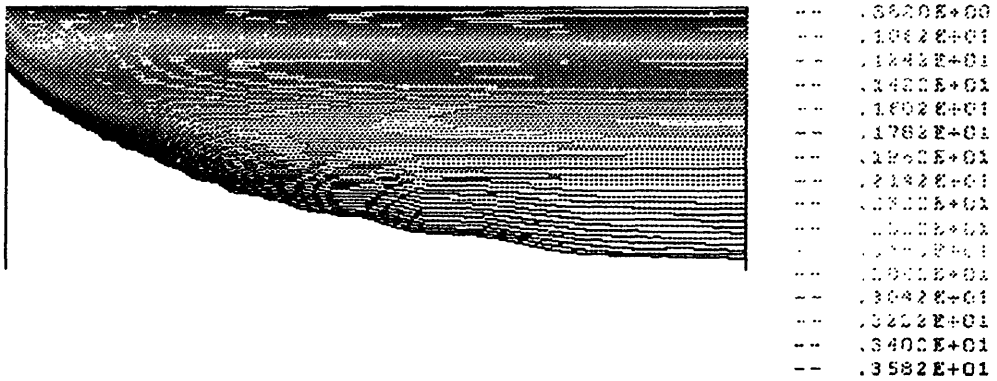

Figure 5-3 Dimensionless Velocity Field within the Melt Pool Under Standard Operating Conditions

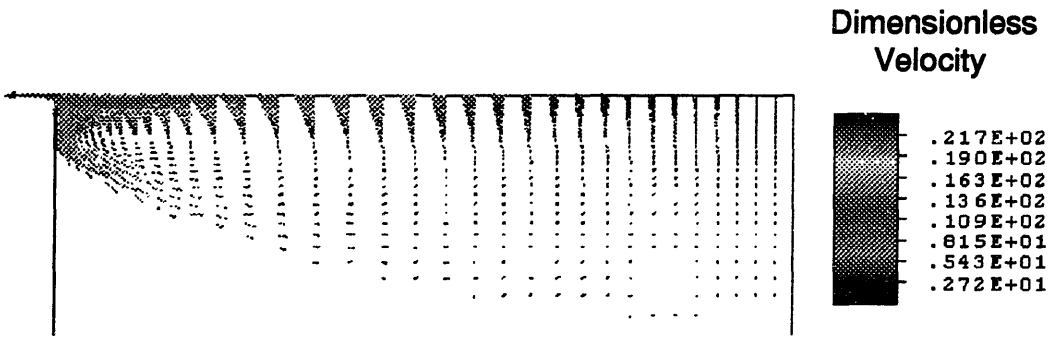

Figure 5-4 Dimensionless Temperature versus Radial Position Across the Melt Pool Free Surface Under Standard Operating Conditions

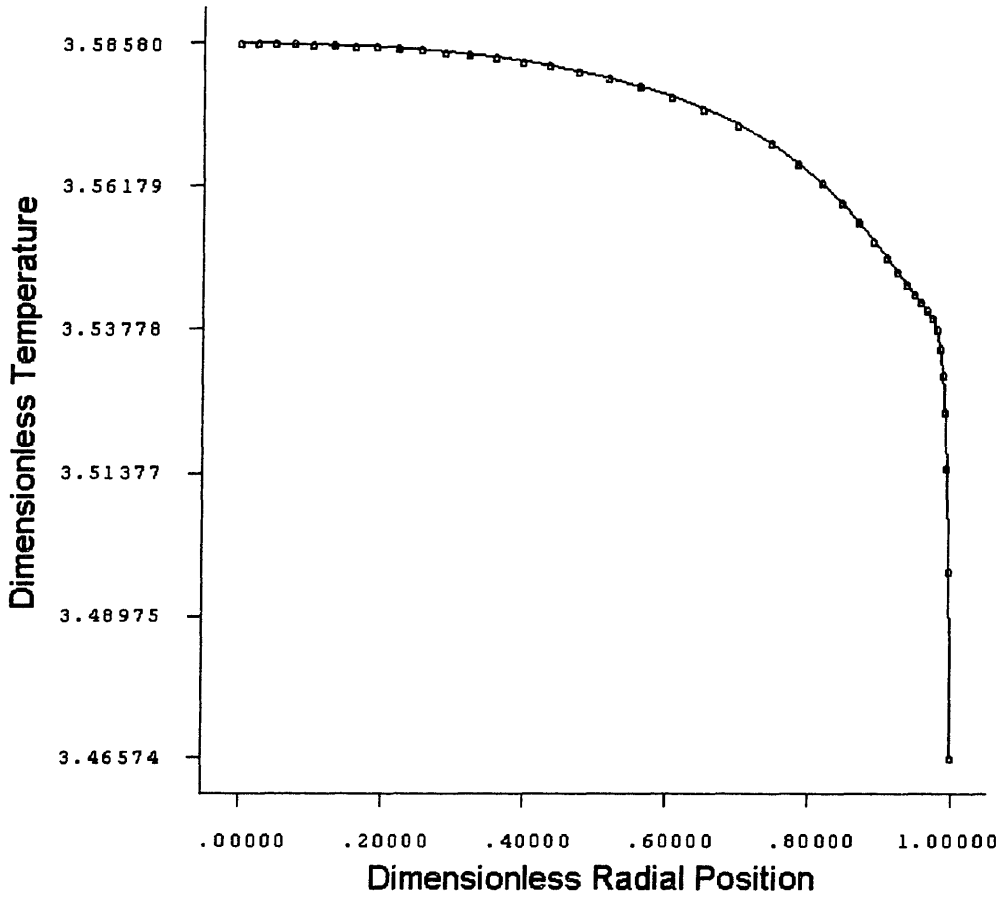

to the melt pool while all negative temperatures correspond to the ingot. A marked change in the isotherm spacing can be detected at the transition between the solid and liquid phases. Note that the temperature gradients within the melt pool are relatively small compared to those in the solid ingot. This is due to the larger conductivity of the molten material, the to decrease in heat flux through the material as energy is consumed in the latent heat of melting, and to convective mixing within the pool.

Figure 5-2, which displays the temperature field in the melt pool only, provides a closer view of this region. Note that the color scale used in Figure 5-2 is different from the one used in Figure 5-1. Towards the lower portion of the melt pool, the shapes of the isotherms resemble those in the solid ingot. Near the top of the pool the isotherms align themselves nearly parallel with its surface and a small, downward dimple in the isotherms is noticeable near the edge of the melt pool. Evidence of the discretized solution underlying these plots is noticeable along the pool's melting front where a slight stair-stepped effect can be seen. Any effect of the fluid motion on the shape of the melting front is not obvious.

Figure 5-3 displays the velocity field within the melt pool. It shows that there is only one flow loop within the melt pool under standard operating conditions. The velocities are largest towards the edge and top of the melt pool. These relatively large velocities explain the small dimple seen in the isotherms in Figure 5-3. They show that the fluid flow conveys hot fluid from the pool's surface downward along its edge towards its bottom. The small dimples seen in Figure 5-2 show that this effect is minor under standard operating conditions. Figure 5-3 also shows that the fluid appears to make a very sharp 90° turn as it flows along the pool's surface and finally reaches the edge of the pool.

Figure 5-4 displays the temperature distribution across the melt pool's free surface only. It shows that temperature drops off smoothly and slowly until it reaches the very edge of the melt pool. Then the temperature drops off quite suddenly over a very small distance. The Marangoni stress due to this large temperature gradient is possibly responsible for the large velocities near the pool's top edge and the sharp turn the fluid takes. However, since temperature changes across the melt pool's entire surface by less than 4%, little emphasis should be placed on the actual shape of the curve shown in Figure 5-4. The temperature changes depicted are rather small for the accuracy of this model. This is the main reason for selecting ΔT_{surf}, the difference between the maximum and minimum pool surface temperatures, as the only quantitative measure of the distribution of temperature across the melt pool's surface.

The first independent dimensionless parameter to be considered in the qualitative analysis is the Nusselt Number based on heat flux, Nu_q. Figures 5-5 and 5-6 show plots of the the melt pool's velocity field for the maximum and minimum values of Nu_q studied, 1840 and 460, respectively. Note that at either

Figure 5-5 Dimensionless Velocity Field for Nu_q=1840

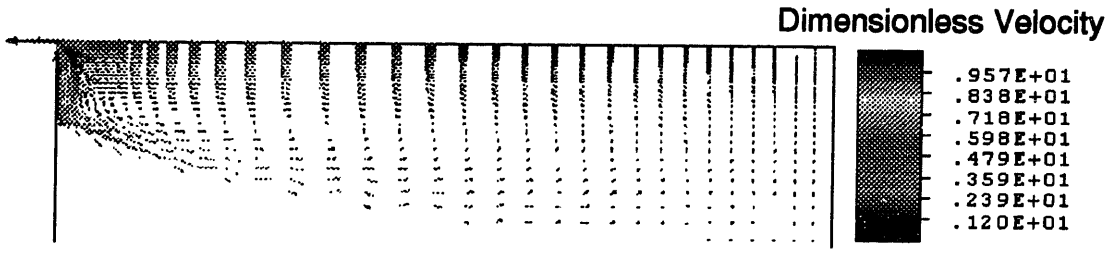

Figure 5-6 Dimensionless Velocity Field for Nu_q=460

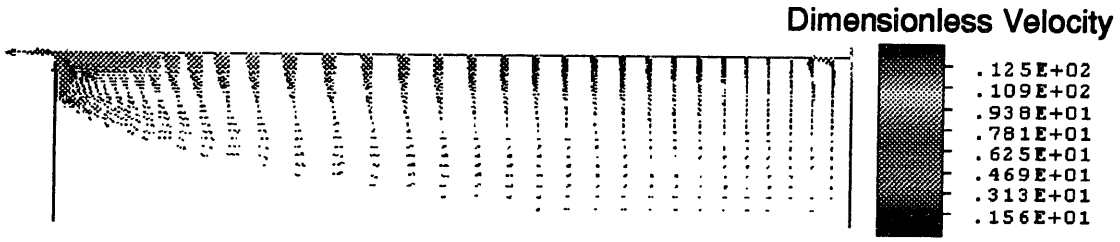

Figure 5-7 Dimensionless Melt Pool Surface Temperature versus Radial Position for Various values of Nu_q

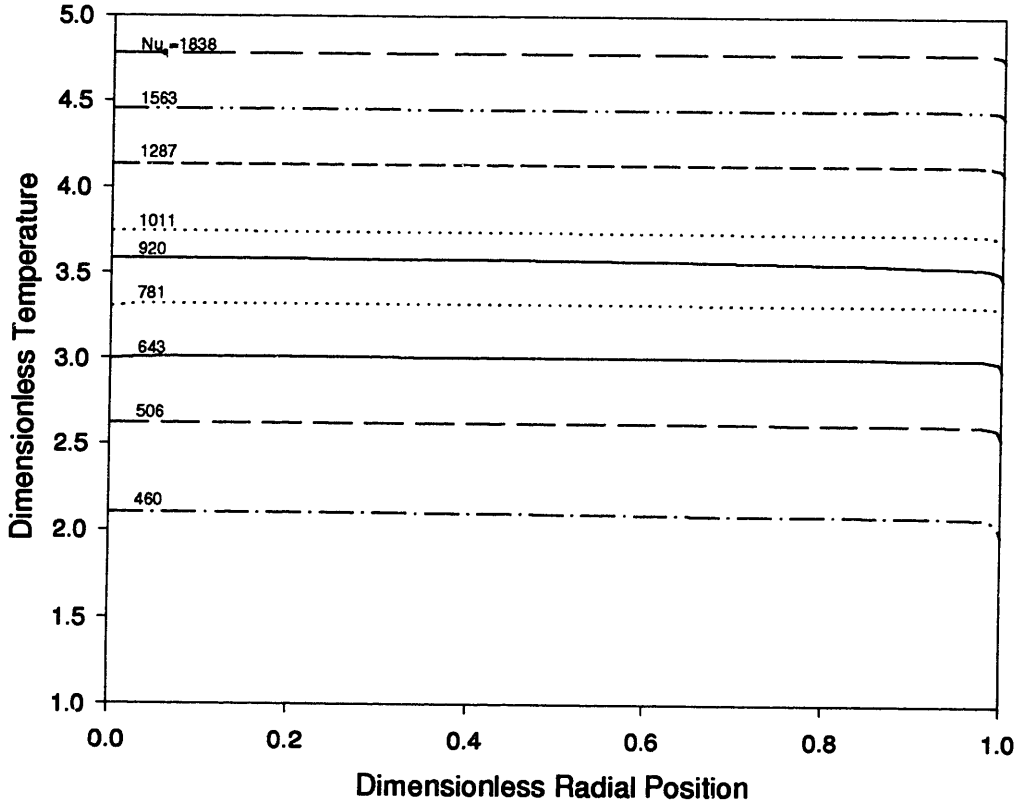

of these extremes, the velocities in the pool are smaller than those at the starting point conditions (Nu_q=920). At Nu_q=1840 the pool appears a little deeper, especially near its edge. At Nu_q=460, the opposite is true. For the most part, however, the velocity field appears very similar to the starting point velocity field. Figure 5-7 shows a plot of dimensionless pool surface temperature versus radial position for various values of Nu_q. Note that the general shape of this temperature distribution does not change much; however, the temperature of the pool's surface increases in general with increasing Nu_q and decreases in general with decreasing Nu_q.

The next independent parameter to consider is Nu_{hc}. Figures 5-8 and 5-9 show plots of the melt pool's velocity field for the maximum and minimum values of Nu_{hc} studied, 9.4 and 0.094, respectively. At Nu_{hc}=9.4, the velocities in the melt pool are, in general, larger than those observed at our starting-point (Nu_{hc}=0.94). The maximum velocity in this pool is 91.3 while velocities in the far-field have values around 10. At our starting-point, the maximum and far-field velocities are 21.7 and 2, respectively. However, when Nu_{hc}=9.4, all of the quick moving fluid is confined to the upper portion of the melt pool's edge. The remainder of the pool's velocities are nearly uniform in magnitude. From our order of magnitude analysis in Appendix B, we know that Marangoni stress can dominate our melt pool when $\Delta T_r/L$ is large (where this ratio is representative of our radial

Figure 5-8 Dimensionless Velocity Field for Nu_{hc}=9.4

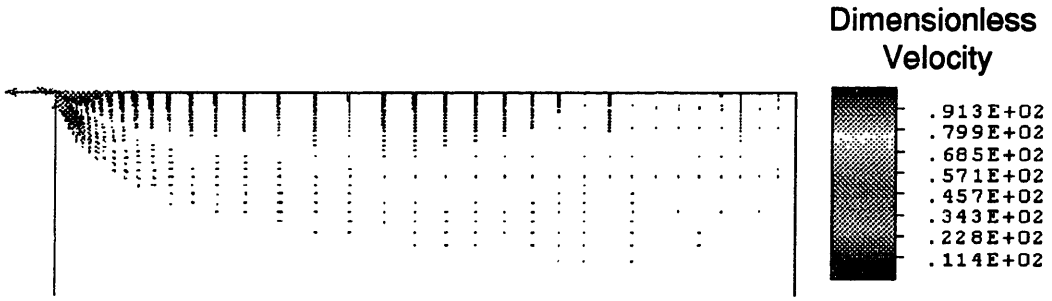

Figure 5-9 Dimensionless Velocity Field for Nu_{hc}=0.094

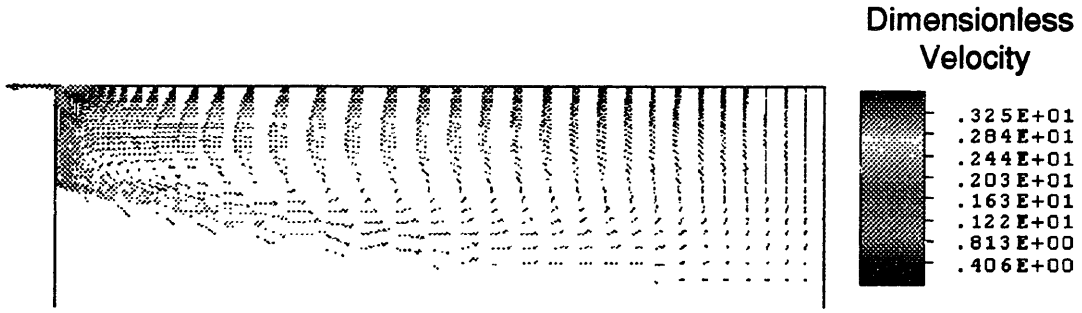

temperature gradient). At large values of Nu_{hc}, greater heat flux through the melt pool's edge causes larger temperature gradients along the pool's surface - especially near the edge of the pool. When Nu_{hc}=9.4, the radial temperature gradients near the pool edge are apparently large enough for Marangoni effects in the corners of the pool to dominate the flow field.

At Nu_{hc}=0.094, the opposite effect occurs. While some large velocities are confined to the pool's upper edge, a bigger loop of relatively large velocities permeates the remainder of the melt pool. Since the heat flux through the pool's edge has been cut down by dropping h_c, the Marangoni stress induced flow near the edge of the pool's surface no longer dominates. The larger loop appears to be a result of natural convection since the top of this loop does not approach the pool's surface where Marangoni stress could come into play. Further, a nearly uniform temperature field near the pool's surface must prevent this loop from affecting the very top of the melt pool. Finally, note that the velocities in the pool at Nu_{hc}=0.094 are, in general, smaller than those in the pool at standard conditions.

Examination of the surface temperature distributions for various values of Nu_{hc} showed that the surface temperature changed very little in the range examined; therefore, no plot of this is provided. This statement was true everywhere except at the very edge of the melt pool's surface where the effects of heat flux into the crucible were felt most. Recall that the largest temperature gradients were seen at the edge of the pool's surface under standard operating conditions. This remained true for all values of Nu_{hc} examined; however, this gradient obviously increased as Nu_{hc} (and the heat flux into the crucible) increased.

The final independent parameter under investigation is the dimensionless standard deviation, σ^*. Figures 5-10 through 5-12 display plots of the temperature field within the melt pool for three values of σ^*: 1.03, 0.833, and 0.25. Figures 5-13 through 5-15 display plots of the corresponding velocity fields. The qualitative analysis of this data indicated that the melt pool might best be characterized by three regimes. In the first regime, the melt pool spans the entire surface of the ingot and is nearly uniform in depth. In the third regime, the melt pool does not span the entire surface of the ingot. The second regime is a transition between the first and third regimes where the pool spans the entire ingot but may appear pinched towards the edge. The three melt pools displayed in Figures 5-10 through 5-15 are good examples of pools from each of the three regimes.

The reason for the pinching effect that may be seen in the second regime is because the YSZ material would solidify near the crucible wall were it not for convective heat transfer within the melt pool. The fast moving fluid along the pool's surface carries hot fluid along with it. The energy in this hot fluid is sufficient to maintain a liquid pool near the crucible. Note that the pinching

Figure 5-10 Dimensionless Temperature Field within the Melt Pool for $\sigma^*=1.03$

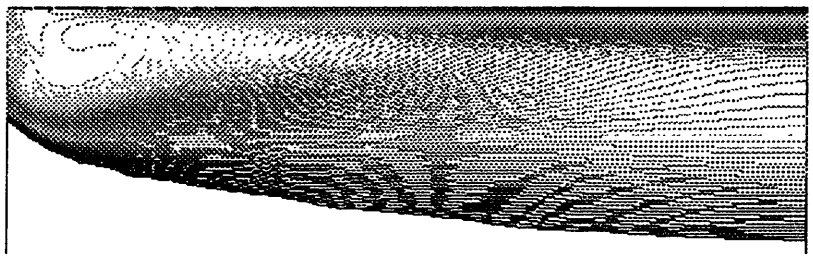

Figure 5-11 Dimensionless Temperature Field within the Melt Pool for $\sigma^*=0.833$

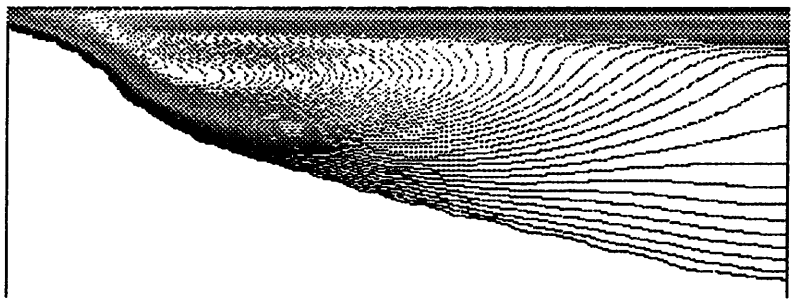

Figure 5-12 Dimensionless Temperature Field within the Melt Pool for $\sigma^*=0.25$

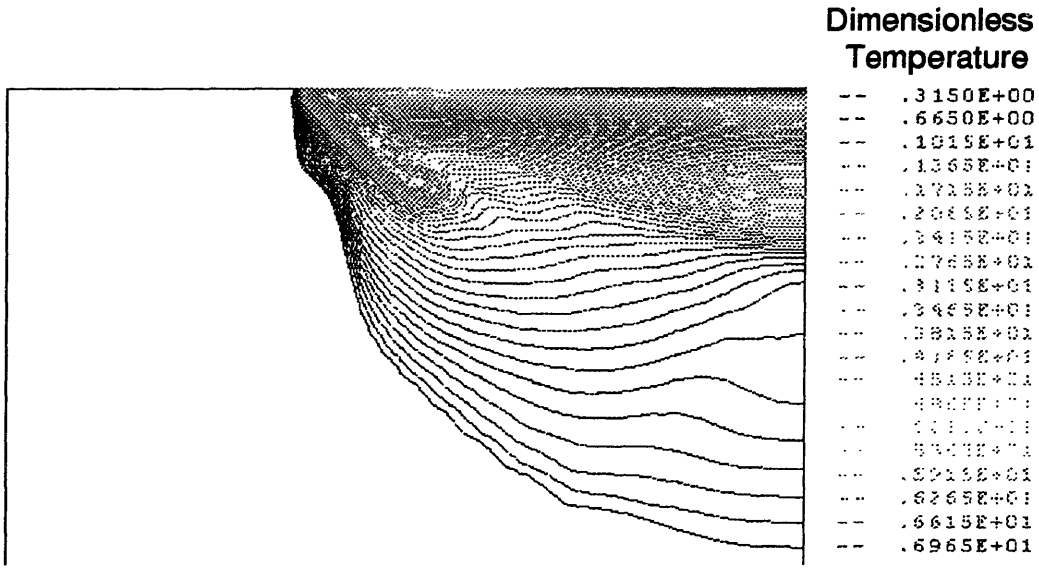

Figure 5-13 Dimensionless Velocity Field within the Melt Pool for $\sigma^*=1.03$

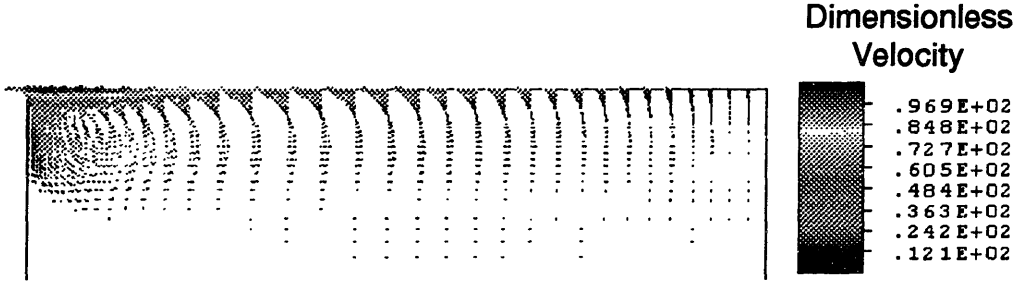

Figure 5-14 Dimensionless Velocity Field within the Melt Pool for $\sigma^*=0.833$

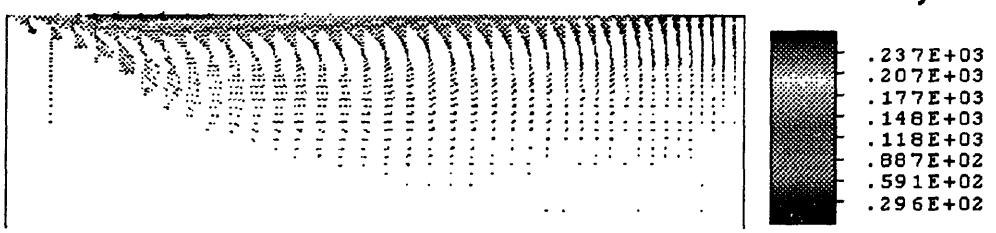

Figure 5-15 Dimensionless Velocity Field within the Melt Pool for σ^*=0.25

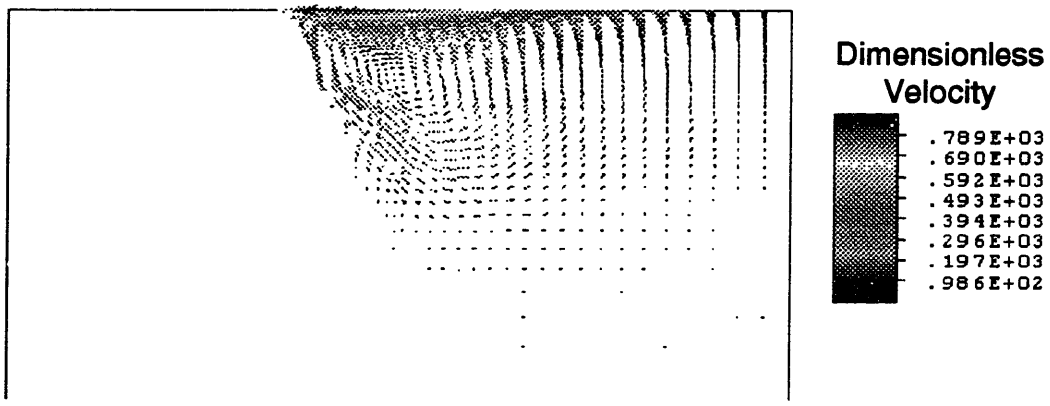

effect begins to disappear with decreasing σ^* before passing into the third regime. It is surmised that the fluid motion within the pool becomes so vigorous that convective heat transfer begins to strongly influence the melt pool's shape. Specifically, the hot fluid carried downward along the outer edge of the pool begins to "burrow" the pool a little deeper.

Dividing the three regimes by σ^* is possible to some extent from the data collected. More experiments along these lines would help to better pinpoint the transition between them. Regardless, the first regime seems to occur when σ^* is greater than 1.0. The third regime is present when σ^* is less than 0.5. The transitional second regime would then fall between values of 1.0 and 0.5 for σ^*. Note that the PVD system being studied currently operates under the first regime. Also note that the third regime is not feasible for the operation of a continuous PVD process. The fluid flow in each of the three regimes is similar in form; however, the velocities in general increase with decreasing σ^*. As more of the electron beam's energy is focused on the center of the pool with decreasing σ^*, the temperature gradients on the pool's surface increase. The Marangoni stress generated is therefore increased along with the melt pool velocities. Also, note that in the first and third regimes the largest velocities are always found at the edge of the melt pool's surface. When pinching is prominent in the second regime, the largest velocities are found on the pool's surface but slightly more towards the centerline. The small area at the pool's edge apparently restricts the fluid flow. Finally, note from the temperature field plots that convective heat transfer is apparent from the swirls seen in the isotherms at all of the values of σ^* tested.

After completing this visual analysis, quantitative results were extracted from the experimental data. The three dependent dimensionless parameters, θ_{avg}, $\dot{m}^*$, and $\Delta\theta_{surf}$, were calculated for each step of every experiment. First, the data collected from the experiments by varying thermophysical properties was used to assess the potential error in this thesis. Then, the data collected from the remaining experiments was used to formulate simple relations between the controllable parameters and the dependent quantities.

First, potential error shall be assessed in the dependent parameters θ_{avg} and $\dot{m}^*$. In the three experiments where Pr, Gr, and St were varied, neither of these dependent dimensionless parameters changed by more than 1%. Recall that in these experiments, the independent thermophysical property parameters were varied over two orders of magnitude. This range should be sufficiently large enough to conclude that very little error is likely to exist in these dependent parameters. Further recall that a few of the steps taken in the Pr experiment did not converge and that the data from these steps was discarded. This decision narrowed the range of Pr investigated to between values of 3.46 and 173. This range should still be sufficiently large enough to assume that θ_{avg} and $\dot{m}^*$ are relatively accurate.

Conversely, the parameter $\Delta\theta_{surf}$ varied significantly over the ranges of Pr, Gr, and St examined. Throughout the experimental simulation varying Pr, $\Delta\theta_{surf}$ saw a maximum value which was 14% greater than that recorded at our starting-point. In the same simulation, $\Delta\theta_{surf}$ saw a minimum value which was 30% below that recorded at our starting-point. In the experimental simulation examining Gr, $\Delta\theta_{surf}$ saw a maximum value which was <1% greater than its "starting-point value" and a minimum value which was 19% smaller. Finally in the numerical simulation examining St, $\Delta\theta_{surf}$ saw a maximum value 6% greater than its "starting-point value" and a minimum value 43% smaller.

If we consider the uncertainty in Pr, Gr, and St to be bounded in the upward direction by an order of magnitude and in the downward direction by another order of magnitude, then the variance seen in $\Delta\theta_{surf}$ due to this uncertainty should be no greater than that experienced in these experimental simulations. Unfortunately, $\Delta\theta_{surf}$ was seen to vary quite significantly as described in the preceding paragraph. Clearly, this parameter is subject to a great deal of uncertainty. In order to gain a more thorough understanding of this parameter, more accurate measurements of the thermophysical properties might be made, or experimental verification of the numerical experiments might be done.

As mentioned above, the three experimental simulations involving the controllable parameters Nu_q, Nu_{hc} and σ^* were used to generate functions which

describe the variation of the three dependent parameters. The process used to generate these functions is fairly simple and is described in detail below.

After extracting θ_{avg}, $\dot{m}^*$, and $\Delta\theta_{surf}$ from the melt pool surface temperature distributions calculated at each load step in these experiments, all of the independent and dependent parameters were normalized with respect to their values at standard operating conditions. This normalized data was then plotted and fit to curves giving us separate expressions for our normalized dependent parameters each in term of a single normalized independent parameter. For example, three expressions could be generated for θ_{avg}:

$$\frac{\theta_{avg}}{\theta_{avg_O}} = f_1\left(\frac{Nu_q}{Nu_{q_O}}\right), \frac{\theta_{avg}}{\theta_{avg_O}} = f_2\left(\frac{Nu_{hc}}{Nu_{hc\,o}}\right), \frac{\theta_{avg}}{\theta_{avg_O}} = f_3\left(\frac{\sigma^*}{\sigma_o^*}\right)$$

where θ_{avg_O} is the value of θ_{avg} at standard operating conditions, Nu_{q_o} is the value of Nu_q at standard operating conditions, etc.

We would like to formulate a single expression for θ_{avg} as a function of all three independent parameters. Note that if we are given a general function of, say, three variables we could write the following:

$$T = f(x_1, x_2, x_3)$$

$$\nabla T = \frac{\partial f}{\partial x_1}\vec{i}_{x_1} + \frac{\partial f}{\partial x_2}\vec{i}_{x_2} + \frac{\partial f}{\partial x_3}\vec{i}_{x_3}$$

$$T(x_1, x_2, x_3) - T_o = \int_{(x_{1_0}, x_{2_0}, x_{3_0})}^{(x_1, x_2, x_3)} \nabla T \cdot d\vec{s}$$

where $d\vec{s} = \vec{i}_{x_1} + \vec{i}_{x_2} + \vec{i}_{x_3}$

$$T(x_1, x_2, x_3) - T_o = \int_{x_{1_0}}^{x_1} \frac{\partial f}{\partial x_1} dx_1 + \int_{x_{2_0}}^{x_2} \frac{\partial f}{\partial x_2} dx_2 + \int_{x_{3_0}}^{x_3} \frac{\partial f}{\partial x_3} dx_3$$

where each of the partials is technically a function of $x_1, x_2, \& x_3$ but we shall approximate them by the single variable derivatives in this manner: $\frac{\partial f(x_1, x_2, x_3)}{\partial x_i} \approx \frac{df_i(x_i)}{dx_i}$

$$T(x_1, x_2, x_3) - T_o \approx \left(f_1(x_1) - f_1(x_{1_o})\right) + \left(f_2(x_2) - f_2(x_{2_o})\right) + \left(f_3(x_3) - f_3(x_{3_o})\right)$$

$$\frac{T(x_1, x_2, x_3) - T_o}{T_o} \approx \frac{f_1(x_1) - T_o}{T_o} + \frac{f_2(x_2) - T_o}{T_o} + \frac{f_3(x_3) - T_o}{T_o}$$

$$\frac{T(x_1, x_2, x_3)}{T_o} \approx \frac{f_1(x_1)}{T_o} + \frac{f_2(x_2)}{T_o} + \frac{f_3(x_3)}{T_o} - 2$$

We can use this template to combine each of our expressions for a dependent variable into a single expression. The step where we approximate the partial derivative allows us make use of our three curve-fit expressions (each in terms of a different independent variable) for each dependent variable. The expressions we generate from this template should be valid as long as our approximations for the partial derivatives are reasonably good. This should be the case for any set of independent parameters that is close to the set that characterizes our starting point.

Our quantitative analysis shall begin using the data for θ_{avg}. Note that θ_{avg} varied by less than 1% when Nu_{hc} was varied to the furthest extremes of the range being examined. It was therefore concluded that θ_{avg} was not dependent upon Nu_{hc} over the range examined. Figures 5-16 and 5-17 show plots of normalized θ_{avg} versus values of the other two normalized controllable parameters, Nu_q and σ^*, respectively.

Figure 5-16 shows that θ_{avg} increases steadily with Nu_q which is an expected result. Figure 5-17 shows that θ_{avg} drops slowly at first and then quite rapidly as σ^* is decreased. This is interesting since the same amount of power is supplied to the ingot, yet its average surface temperature drops. Achieving a drop in average surface temperature is apparently possible simply by concentrating the electron beam's energy more towards the center of the ingot.

Figures 5-16 and 5-17 also display curves that have been fit to this normalized data. These functions are:

$$\frac{\theta_{avg}}{\theta_{avg\,o}} = 53\left(\frac{Nu_q}{Nu_{qo}}\right)^{0.011} - 52$$

$$\frac{\theta_{avg}}{\theta_{avg\,o}} = -0.25e^{\left(\frac{0.033}{(\sigma^*/\sigma^*_o)^2}\right)} + 68$$

These three functions can combined as described above to obtain a comprehensive function which describes the variation of θ_{avg} with both of Nu_q and σ^*:

$$\frac{\theta_{avg}}{\theta_{avg\,o}} = \left[53\left(\frac{Nu_q}{Nu_{qo}}\right)^{0.011} - 52\right] + \left[-0.25e^{\left(\frac{0.033}{(\sigma^*/\sigma^*_o)^2}\right)} + 68\right] - 1$$

Note that we have implicitly used a function for θ_{avg} in terms of Nu_{hc} in formulating this expression. This function is simply $\frac{\theta_{avg}}{\theta_{avg_o}} = 1$.

Analysis was next performed on the dependent dimensionless parameter $\Delta\theta_{surf}$. Note that this parameter was found to vary significantly with all three controllable parameters. Figures 5-18, 5-19, and 5-20 show plots of normalized $\Delta\theta_{surf}$ versus values of normalized Nu_q, Nu_{hc}, and σ^*, respectively. Figure 5-18 shows that $\Delta\theta_{surf}$ decreases with Nu_q. Thus, increasing the beam's power decreases the variation in temperature (and vapor flux) across the pool's surface. Figure 5-19 shows that $\Delta\theta_{surf}$ increases quite steadily with Nu_{hc}. In order to minimize variations in temperature and vapor flux, Nu_{hc} should be kept to a minimum. Conversely, in order to maximize these variations we should make Nu_{hc} as large as possible. Figure 5-20 shows that $\Delta\theta_{surf}$ increases significantly for very small values of σ^*. This is another fairly intuitive result although the exponential-like behavior might not have been expected.

These three plots also show curve fits similar to those found in Figures 5-16 and 5-17. The functions which describe these curves are:

$$\frac{\Delta\theta_{surf}}{\Delta\theta_{surf_o}} = -0.89e^{\left(\frac{0.55}{(Nu_q/Nu_{q_o})}\right)} - 0.54$$

$$\frac{\Delta\theta_{surf}}{\Delta\theta_{surf_o}} = 0.62\left(\frac{Nu_{hc}}{Nu_{hc\,o}}\right)^{0.86} + 0.38$$

$$\frac{\Delta\theta_{surf}}{\Delta\theta_{surf_o}} = 4000e^{\left(\frac{0.00025}{(\sigma^*/\sigma^*_o)^2}\right)} - 4000$$

Again, these equations can be combined and simplified to form a single comprehensive formula which describes $\Delta\theta_{surf}$'s dependence upon each of the controllable variables:

$$\frac{\Delta\theta_{surf}}{\Delta\theta_{surf\,0}} = \left(-0.89e^{\left(\frac{0.55}{Nu_q/Nu_{q_o}}\right)} - 0.54\right) + \left(0.62\left(\frac{Nu_{hc}}{Nu_{hc\,o}}\right)^{0.86} + 0.38\right) + \left(4000e^{\frac{0.00025}{(\sigma^*/\sigma^*_o)^2}} - 4000\right) - 2$$

Finally, the data for $\dot{m}^*$ was subjected to the same analysis. Similar to the case with θ_{avg}, $\dot{m}^*$ was found to vary less than 1% when Nu_{hc} was varied to the furthest extremes of the range being examined. It was therefore concluded that $\dot{m}^*$ was not dependent upon Nu_{hc} over the range examined. Figures 5-21 and 5-22 display plots of normalized $\dot{m}^*$ versus values of normalized Nu_q and σ^*.

Figure 5-21 shows that $\dot{m}^*$ increases steadily with Nu_q as was expected. Figure 5-22 shows that $\dot{m}^*$ increases rapidly near extreme low values of σ^*. This is an interesting result since θ_{avg} was found to decrease for these values of σ^*. This must be a result of the nonlinear dependence of evaporation rate upon temperature. The evaporation occurring from the melt pool's center (where the temperature is extremely high) apparently more than compensates for the low evaporation rates near the pool's edge.

The curve fits shown in Figures 5-21 and 5-22 are described by the following functions:

$$\frac{\dot{m}^*}{\dot{m}^*_o} = 1.3\left(\frac{Nu_q}{Nu_{q_o}}\right)^{1.2} - 0.3$$

$$\frac{\dot{m}^*}{\dot{m}^*_o} = 0.11e^{\left(\frac{0.24}{(\sigma^*/\sigma^*_o)^2}\right)} + 0.86$$

These equations can be combined and simplified to produce the following relation:

$$\frac{\dot{m}^*}{\dot{m}^*_o} = \left(1.3\left(\frac{Nu_q}{Nu_{q_o}}\right)^{1.2} - 0.30\right) + \left(0.11e^{\left(\frac{0.24}{(\sigma^*/\sigma^*_o)^2}\right)} + 0.86\right) - 1$$

where again we assume that our third expression for $\dot{m}^*$ in terms of Nu_{hc} could be written as $\frac{\dot{m}^*}{\dot{m}^*_o} = 1$ and used in the template discussed above.

Figure 5-16 Normalized θ_{avg} versus Normalized Nu_q

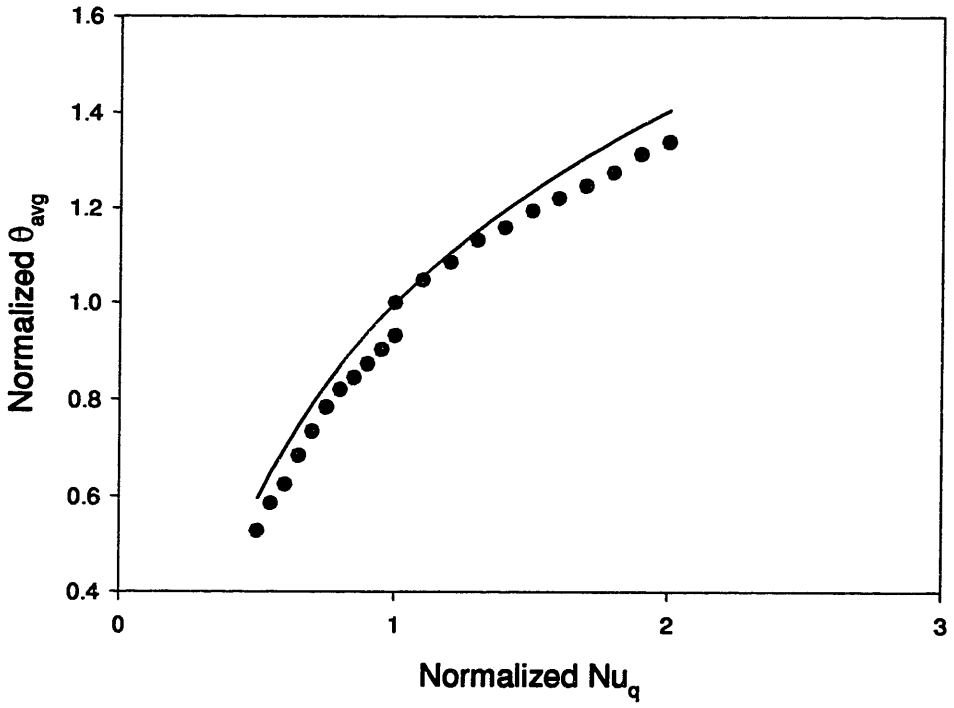

Figure 5-17 Normalized θ_{avg} versus Normalized σ^*

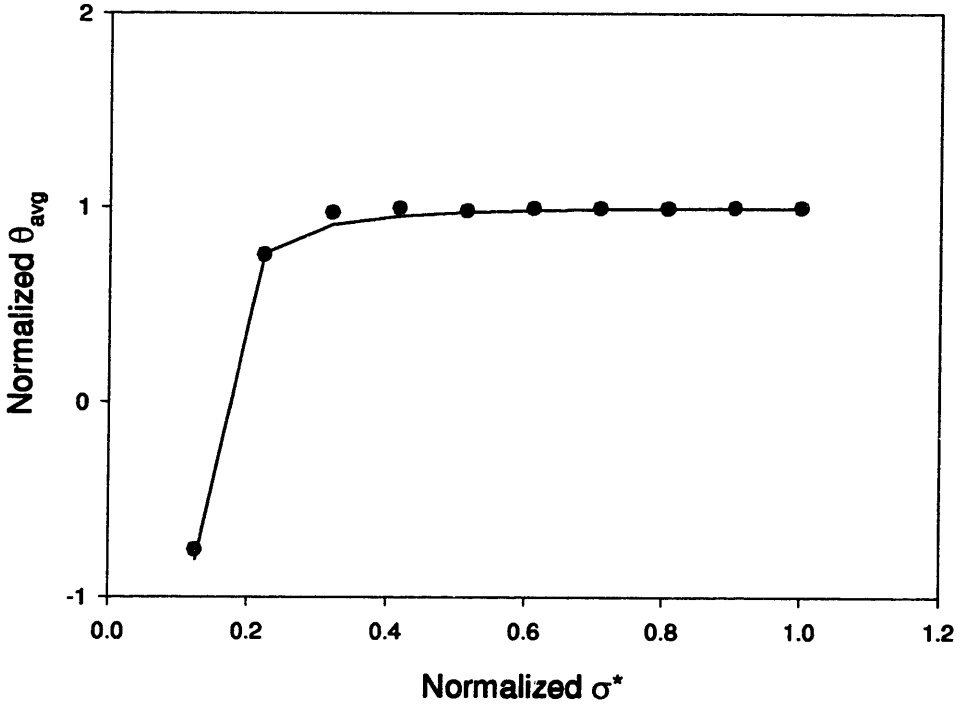

Figure 5-18 Normalized $\Delta\theta_{surf}$ versus Normalized Nu_q

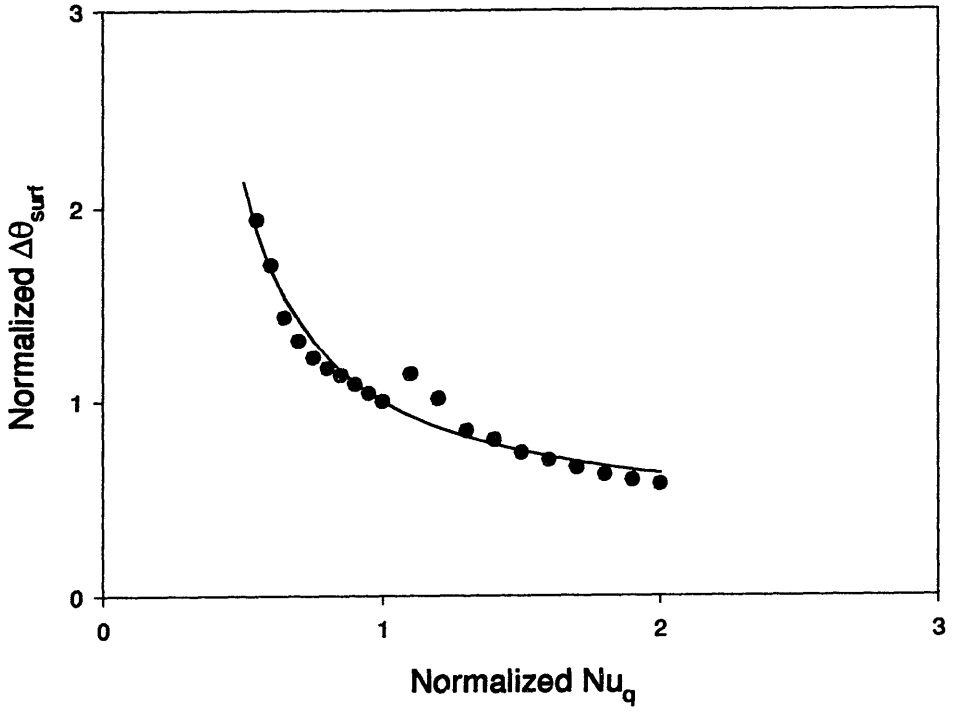

Figure 5-19 Normalized $\Delta\theta_{surf}$ versus Normalized Nu_{hc}

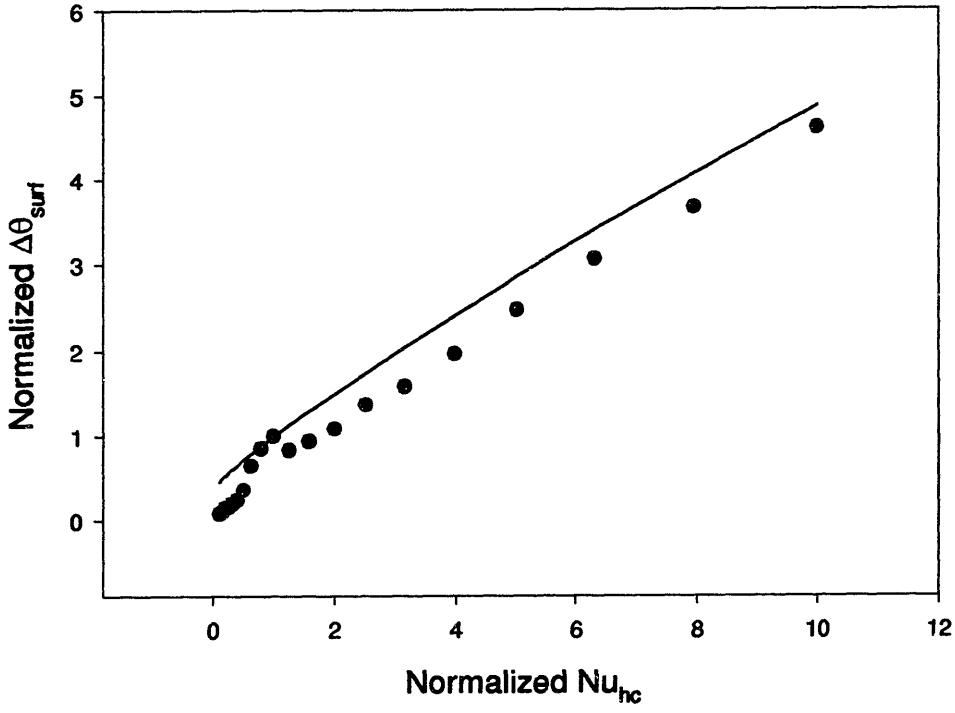

Figure 5-20 Normalized $\Delta\theta_{surf}$ versus Normalized σ^*

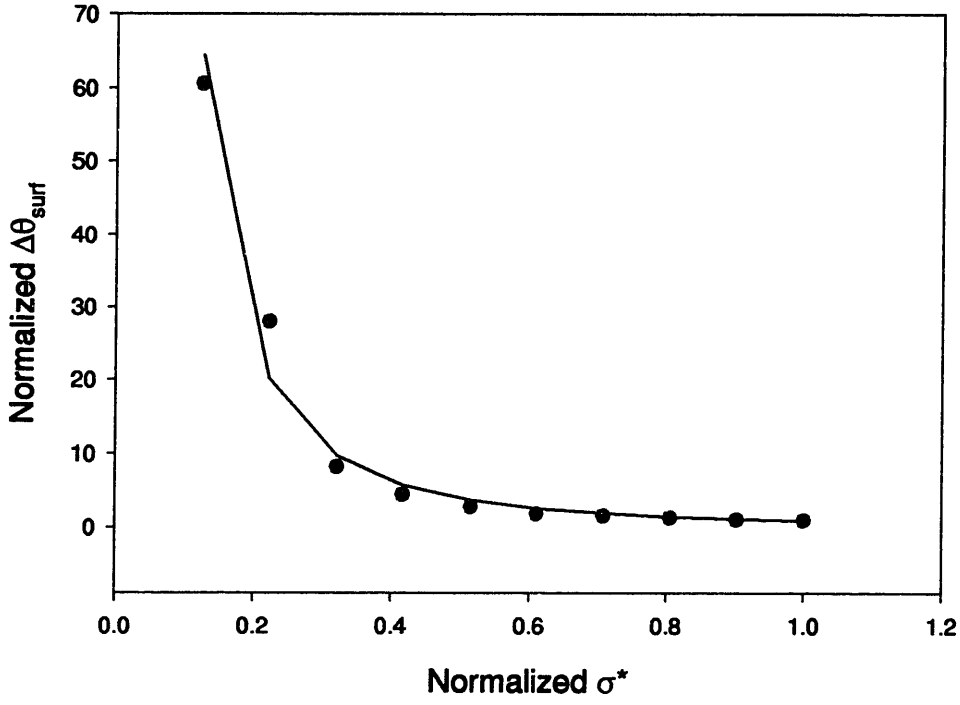

Figure 5-21 Normalized m* versus Normalized Nu_q

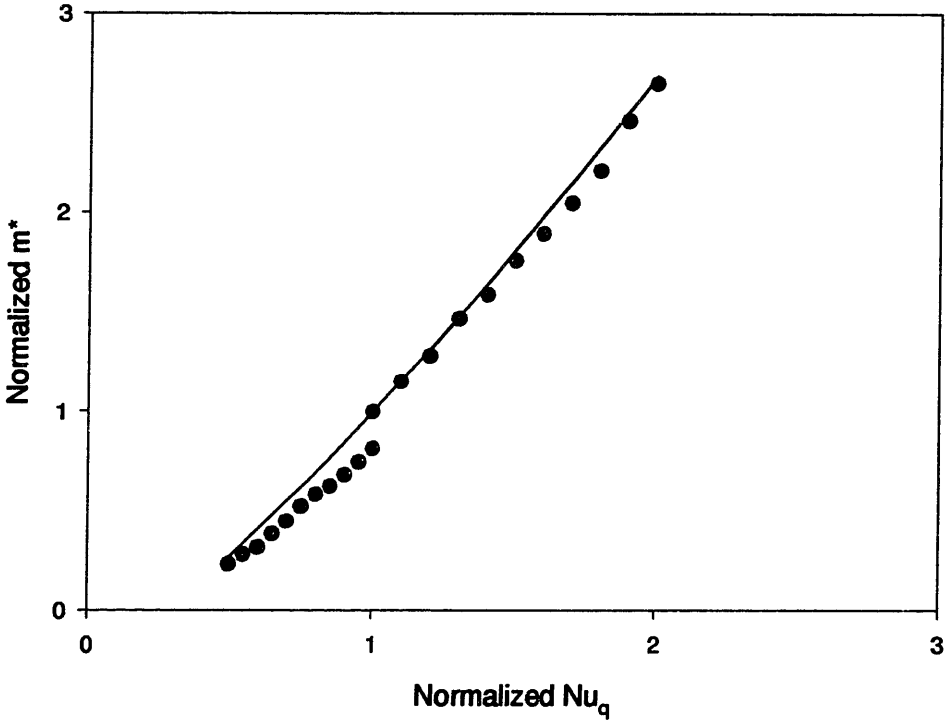

Figure 5-22 Normalized m* versus Normalized σ*

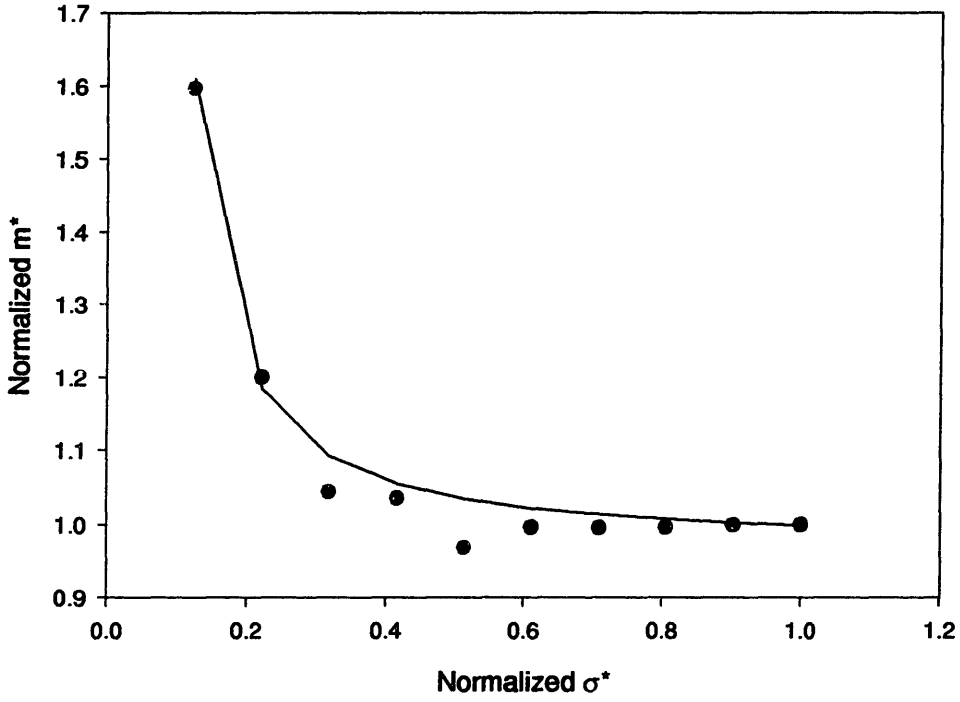

Recall that the main objective of this study was to aid in better controlling the overall PVD process. Although a detailed study of the vapor transport and deposition processes is necessary to make full use of all the data generated from this study, the results obtained from the qualitative and quantitative analyses presented above are themselves of potential use in controlling the PVD process.

Perhaps the most useful of these results is the relation which describes the total vapor flow rate with respect to each of the controllable parameters. This relation could be used to adjust the ingot feed rate to accommodate changes in these parameters. This adjustment would aid in maintaining a steady pool at all times. In addition, it would remove the only remaining manual adjustments needed in this process. Currently, the melt pool's free surface level is controlled according to a visual inspection of the melt pool through a video system. These adjustments are made according to human judgment; therefore, they prevent a particular PVD process from being exactly duplicated time and time again. However, such exact duplication is necessary to assure that the coatings being manufactured are of consistent quality.

Another result of great use would be the relation describing the average melt pool temperature. Since the visual inspection of the melt pool solutions suggested that the melt pool was nearly isothermal over most of its surface area under most conditions, the average melt pool temperature could be used to

provide a good approximation of the heat transfer being radiated from the melt pool. This heat transfer makes a major contribution to the temperature of the hardware being coated. Since the hardware temperature is important to the quality of the TBCs being manufactured, an understanding of this heat transfer is vital to properly controlling the PVD process. By using the relation for average pool surface temperature to calculate this heat transfer, intelligent decisions can be made regarding changes to the controllable parameters. Changes which would affect the hardware temperature adversely could be avoided and changes which would aid in maintaining a proper hardware temperature could be anticipated. Of course, altering the melt pool's temperature so as to affect its heat transfer contribution to the hardware would ultimately affect the vapor flow rate from the melt pool. These effects would be predictable through the vapor flow relation discussed previously.

The relation which describes the variation of $\Delta\theta_{surf}$ is less useful than the other two relations until a more detailed study of the vapor transport and deposition processes is undertaken. This dependent parameter was chosen to represent the variation of temperature and vapor flux across the melt pool surface. These features of the melt pool are expected to influence the distribution of vapor flux throughout the deposition chamber and the temperature of the vapor flux approaching the coated hardware. And while the exact influence of each of the dependent parameters upon TBC quality needs to be determined by additional study of the rest of the PVD process, this parameter's influence is a little less clear than the other two. It is likely that varying $\Delta\theta_{surf}$ will have a strong influence on the locations in the deposition chamber where acceptable TBCs can be produced.

In the absence of further computational study, it might be useful to study the effect of these three parameters on TBC quality through a series of actual experiments. An exact understanding of how conditions in melt pool affect TBC quality could be obtained through these experiments. Then the PVD process could be better controlled by monitoring the melt pool. Intelligent changes in the melt pool's characteristics could be made during a PVD process in order to improve TBC quality. The qualitative understanding and functional relations obtained from this research would provide the means for generating a melt pool with the desired characteristics.

6.0 Conclusions

A computational study examining the melt pool and ingot during a PVD process was performed. This study provided a general understanding of the physics occurring within the melt pool and specific relations between melt pool characteristics and controllable parameters. In addition, an error analysis provided an assessment of the quality of these results given the uncertainty in the thermophysical properties used to model this process.

Under standard operating conditions, the melt pool was observed to contain a single loop of circulating fluid. This circulation somewhat affected the temperature distribution within the pool. At the surface of the pool, the temperature was greatest in the center. The pool surface temperature dropped of slowly with increasing r until the very edge of the pool is reached. At this point, the temperature drops of quite rapidly. The effects of varying the beam power, the heat transfer coefficient, and the beam distribution were noted in Chapter 5.0.

Three functions were generated which describe the relationships between three scalar quantities which characterize the melt pool and three controllable parameters. These functions are as follows:

$$\frac{\theta_{avg}}{\theta_{avg\,o}} = \left[53\left(\frac{Nu_q}{Nu_{q_o}}\right)^{0.011} - 52\right] + \left[-0.25e^{\left(\frac{0.033}{(\sigma^*/\sigma^*_o)^2}\right)} + 68\right] - 1$$

$$\frac{\Delta\theta_{surf}}{\Delta\theta_{surf\,0}} = \left(-0.89e^{\left(\frac{0.55}{Nu_q/Nu_{q_o}}\right)} - 0.54\right) + \left(0.62\left(\frac{Nu_{hc}}{Nu_{hc\,o}}\right)^{0.86} + 0.38\right) + \left(4000e^{\frac{0.00025}{(\sigma^*/\sigma^*_o)^2}} - 4000\right) - 2$$

$$\frac{\dot{m}^*}{\dot{m}^*_o} = \left(1.3\left(\frac{Nu_q}{Nu_{q_o}}\right)^{1.2} - 0.30\right) + \left(0.11e^{\left(\frac{0.24}{(\sigma^*/\sigma^*_o)^2}\right)} + 0.86\right) - 1$$

These functions and the understanding of the melt pool gained from this research could aid in the control of the PVD process. Further research is necessary to determine the exact influence of these three dependent parameters upon TBC quality. Once this research is complete, the characteristics of the melt pool can be manipulated to benefit the PVD process. This research should provide the ability to generate a desired melt pool by intelligently altering the operating conditions of this system.

The quantitative results obtained from this research are likely to contain some degree of error in them due to the uncertainty in the thermophysical properties

used. Fortunately, both θ_{avg} and $\dot{m}^*$ were relatively insensitive to variations in the properties. Results pertaining to these quantities should be quite accurate. The third parameter $\Delta\theta_{surf}$ is much more sensitive to the properties of the melt pool. Results pertaining to this quantity contain a great deal more uncertainty. They should be followed up by additional thermophysical property research or experimental verification.

Appendix A:

Thermophysical Property Summary

After a thorough literature review, a summary of the thermophysical properties of YSZ has been compiled. Since YSZ can contain various amounts of its stabilizing species, Yttria (Y_2O_3), it is necessary to specify that the YSZ of interest contains 7% (wt.) Yttria. As mentioned in the main body of this text, the properties of pure liquid Zirconia (ZrO_2) shall be substituted for the properties of molten YSZ. And while the characteristics of YSZ and ZrO_2 have been studied extensively, it was not possible to locate all of the properties necessary for this research. In these instances the properties of a closely related material, namely Alumina (Al_2O_3), have been researched to provide substitutes.

The most commonly accepted melting temperature for pure Zirconia is 2715°C. For stabilized Zirconia this temperature should be slightly lower. [2] The phase diagram of the ZrO_2 - Y_2O_3 system shows a mushy zone which, for small amounts of Yttria, is essentially centered around the melting point of pure Zirconia. At 7%(wt.) Y_2O_3, the width of this mushy zone is approximately 75°C.[3] This implies a liquidus at about 2678°C and a solidus at about 2753°C.

The vapor pressure of Zirconia has been collected from several sources. Ryshkewitch published an expression for vapor pressure as a function of absolute temperature:

$$\log(P_{atm}) = -34383/T - 7.98E^{-}4T + 11.98$$

which was fit to experimental data in the range 2013K to 2293K. [2] From this formula, Zirconia is determined to develop a vapor pressure of 3.4E-4 torr at 2060K. However, Margrave published a table of vapor pressures for Zirconia at various temperatures:

Table A1: Vapor Pressure Data for Zirconia

Vapor Pressure (torr)	10^{-6}	10^{-5}	10^{-4}	10^{-3}	10^{-2}	10^{-1}	10^{0}
Temp. (K)	2060	2203	2350	2512	2679	2858	3048

which disagree with the formula shown above. [4] A third publication provides the vapor pressure of Zirconia as:

$$\log(P_{atm}) = -4.1176E4/T + 10.088$$

which is more or less in agreement with the Margrave data. [5] It shall be assumed that the third expression is correct.

The molecular weight of pure Zirconia is 123.223 kg/ kmol and of pure Yttria is 225.810 kg/kmol. [6] The heats melting and vaporization for Zirconia are 706.3 kJ/kg and 5069.6 kJ/kg respectively. [7]

The theoretical full density, ρ_{theor}, of solid 7.0%(wt.) Y_2O_3 stabilized ZrO_2 is 6 g/cm^3. The actual density, ρ_{actual}, of a sample of a YSZ ingot from Chromalloy Turbine Technologies in Middletown, NY was determined to be approximately 4.5 g/cm^3 from measurements of its mass and volume.[8] Since porosity, ω, can be estimated by the relation $1-\rho_{actual}/\rho_{theor}$, the estimated porosity of this sample was 25%. Porosity is an important quantity in the determination of several thermal transport properties (e.g. thermal conductivity, specific heat, and thermal diffusivity).

Porosity is only one of several microstructural characteristics that affect the thermal transport properties of YSZ and materials like it. The conduction of heat in polycrystalline, multiphase materials such as YSZ can be affected by four such factors: the dimensions of the material's grains, crystal structure, impurities, and porosity. Some specific effects of each of these factors should be quickly discussed before presenting any raw thermal transport property data.

For example, grain dimensions could influence the thermal conductivity of polycrystalline, multiphase materials by reducing the mean free path of their thermal energy carriers (e.g. phonons, photons, and electrons). However, since the mean free path in metal oxides is generally smaller than their grain size, crystal structure is usually more influential on the mean free path than grain size. Note that at low temperatures the mean free path in metal oxides may become equal to their grain size. At these temperatures the grain size of YSZ could start to influence its thermal transport properties.[10]

With respect to crystal structure, it has been shown that the cubic phase of ZrO_2 has a smaller thermal diffusivity than the monoclinic phase which, in turn, has a smaller diffusivity than the tetragonal phase. Further, it has been most of the variation of Zirconia's thermal diffusivity with respect to crystal structure can be attributed to the amount of cubic phase present. At any given temperature, the amount of Yttria stabilizer present in YSZ determines the relative amounts of Zirconia's phases. Thus, the amount of stabilizer present also has a strong influence on the thermal diffusivity.

The crystal structure of Zirconia also influences the temperature dependence of the thermal transport properties. It has been shown that the thermal diffusivity of monoclinic Zirconia decreases by a factor of three from 25°C to 1000°C. In this temperature range, phonons are the primary thermal energy carriers. The drop seen in monoclinic Zirconia's thermal diffusivity is a result of the temperature dependence of its phonon mean free path which is controlled primarily by phonon-phonon interactions. It has also been shown that the thermal diffusivity of cubic Zirconia varies by no more than 30% over the same range of temperatures. This occurs because the phonon mean free path in cubic Zirconia is controlled primarily by lattice defects. This effect surpresses the influence of the temperature dependence of the phonon-phonon interactions.

It is interesting to note that the specific heat of YSZ shows no significant dependence on stabilizer content or phase composition. This finding is useful because it allows us to directly use specific heat data for Zirconia with different amounts and types of stabilizers than we are considering in our research. [11]

As stated above, there are two more microstructural characteristics that could affect the thermal transport properties of YSZ. Impurities are another potential influence. Little information could be found regarding particular impurities and their effect on YSZ properties so I shall not consider them any further. Porosity was the final characteristic of interest. The effect of porosity on thermal conductivity has been well studied. There are many models which attempt to predict an effective thermal conductivity given the conductivity of a "fully dense" material and its porosity. Some useful examples are as follows:

Model by Bruggeman $$\frac{k_{eff}}{k_m} = (1-\omega)^{1.5} \qquad \omega > 10\%$$

Model by Maxwell-Eucken $$\frac{k_{eff}}{k_m} = \frac{1-\omega}{1+0.5\omega}$$

Model by Russell $$\frac{k_{eff}}{k_m} = \frac{1-\omega^{0.66}}{1+\omega-\omega^{0.66}}$$

where k_{eff} is the effective thermal conductivity, k_m is the conductivity of the "fully dense" material, and ω is porosity. At high temperatures it may be necessary to use more complex models which account for radiation through the pores. [10]

Unfortunately, the effects of all the microstructural characteristics mentioned above on each of the thermal transport properties required have not been uncovered, or perhaps even studied, at this point. This is unfortunate because much of the property data available has been measured for pure Zirconia or YSZ with a different microstructure than the YSZ of interest in this research. This being said, a summary of the available data shall continue with comments on its applicability to this research.

Pawlowski and Fauchais provide tables with the thermal conductivity and diffusivity of thermally sprayed YSZ coatings. Their data spans a temperatures range from 600K to 1400K and comes from YSZ with various amounts of stabilizer. One sample contained 7.25% (wt) Y2O3 but was only 8% porous. [10] Although the conductivity data could be easily corrected to fit our needs, it is unclear how to correct the diffusivity data. Fortunately, some thermal conductivity data for YSZ of the exact composition and porosity we require has been provided to us by Hague. [12] The data which spans temperatures from 300K to 1673K can be described accurately by a second order polynomial:

$$k(T) = 1.241 - 1.284E^{-3}T + 6.186E^{-7}T^2$$

YSZ conductivity data above 1673K is limited. At high temperatures, Touloukian provides data for pure Zirconia (about 6% porosity) and CaO stabilized Zirconia (fully

dense). Both sets of data span a temperature range from about 1400K to 2300K.[9] At 1473K, Hague reports that the YSZ of interest has a conductivity of 0.744 W/ mK. The pure Zirconia data from Touloukian provides a value of 0.79 W/ mK when corrected to 36% porosity (the porosity reported by TransTech) using the Bruggeman model. Although pure Zirconia has a very different microstructure than YSZ, there is only a 6% difference between these conductivity values. Considering the great deal of scatter in the Zirconia data this is a pretty good correlation. If pure Zirconia is assumed to convey the same thermal conductivity temperature dependence as the YSZ of interest in this temperature range, then the Hague and Touloukian data sets could be combined and conductivity could be expressed in a piecewise fashion as follows:

$$k(T) = 1.241 - 1.284E^{-3}T + 6.186E^{-7}T^2 \qquad (300K<T<1250K)$$
$$k(T) = 4.341E^{-4}T + 5.98E^{-2} \qquad (1250K<T<2988K)$$

See Figure 1 for a plot of the raw thermal conductivity data and these expressions.

Figure A1: YSZ's Thermal Conductivity versus Temperature

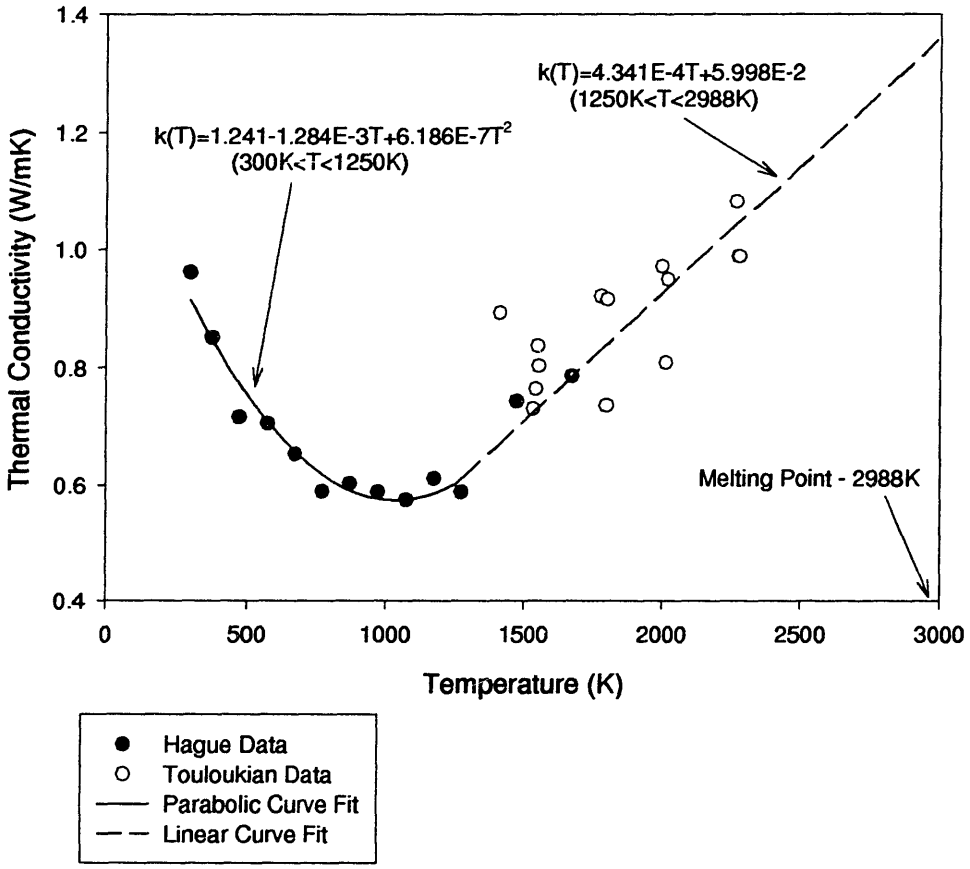

As was mentioned above, the specific heat of YSZ was not found to depend upon stabilizer content or phase composition. Consequently, specific heat data for pure Zirconia could be substituted for YSZ without any corrections. Touloukian has published data sets for pure Zirconia's specific heat over various temperature ranges. By collecting data from three particular experiments we obtain a set which spans from 54K to 2755K. Note that although the data was taken from samples with different types and amounts of stabilizers it pieces together smoothly, reflecting specific heat's invariance with respect to these parameters.[9] The only remaining caveat is that the Touloukian data was taken from "fully dense" samples. Since no correction should be necessary for the porosity of the samples, the specific heat data can then be expressed in a piecewise fashion as follows:

$$c_p(T) = -61.028 + 2.627T - 3.847E^{-3}T^2 + 2.558E^{-6}T^3 - 7.526E^{-10}T^4 + 8.288E^{-14}T^5 \quad (50K<T<1600K)$$

$$c_p(T) = -47.44 + 0.4723T \quad (1600K<T<2988K)$$

See Figure A2 for a plot the raw specific heat data and this expression.

Figure A2: YSZ's Specific Heat versus Temperature

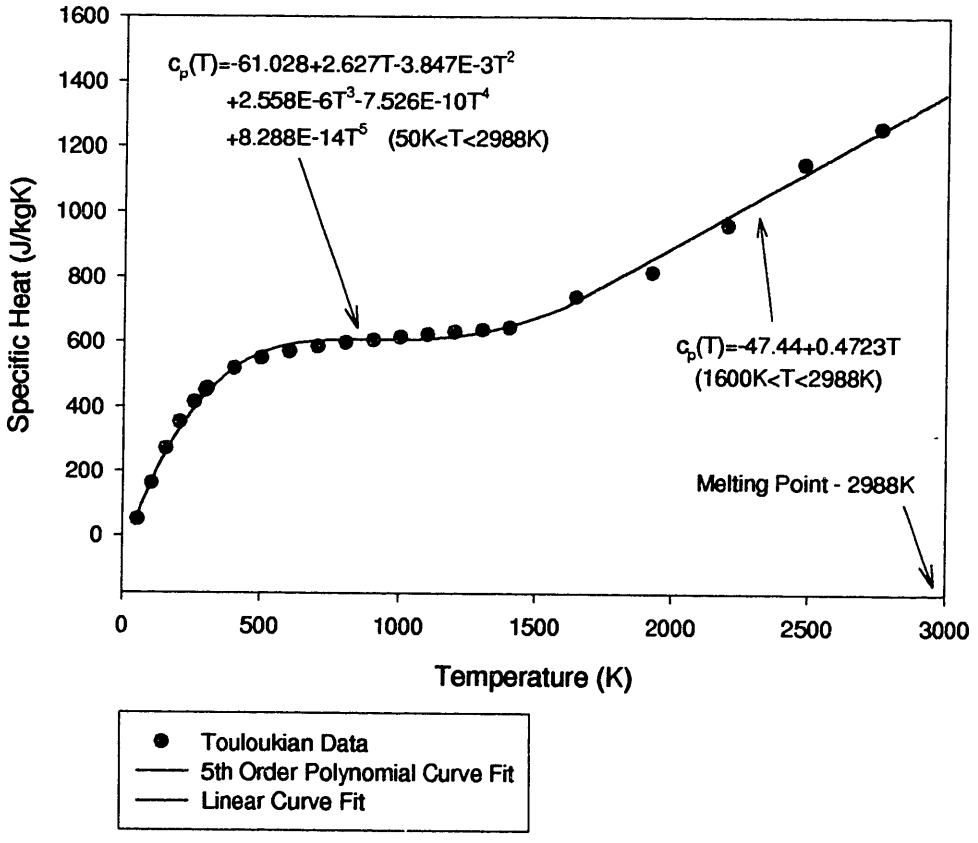

The final thermal transport property, thermal diffusivity, can be calculated according to its definition:

$$\alpha = k/rc_p$$

where α is thermal diffusivity, k is thermal conductivity, r is density, and c_p is specific heat. Using the expressions for thermal conductivity and specific heat above and a constant density value of 3.8 g/cm^3, we can compute values for diffusivity at any temperature from 300K to 2988K. See Figure A3 for a plot of calculated thermal diffusivity values versus temperature.

Figure A3: YSZ's Calculated Thermal Diffusivity versus Temperature

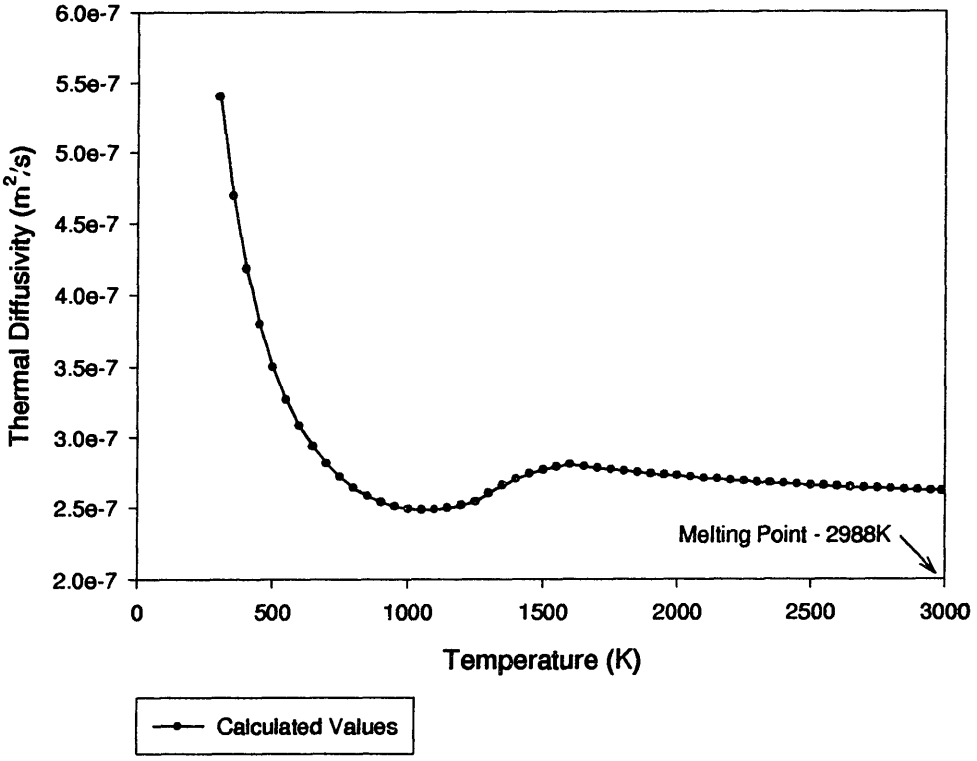

Qualitatively, the thermal diffusivity values that we calculated make sense. The initial and rapid decrease in thermal diffusivity can be attributed to relative changes in the material's phases with temperature and to the temperature dependence of the phonon mean free path. As mentioned above, the three phases of Zirconia, in order of decreasing thermal diffusivity, are monoclinic, tetragonal, and cubic. As temperature increases, 7%(wt.) Y_2O_3 stabilized ZrO_2 changes from a mix of monoclinic and cubic phases to a mix of tetragonal and cubic phases and finally to pure cubic phase before melting. This characteristic is partially responsible for the initial drop in diffusivity and

the general decrease observed over all temperatures. It was also mentioned above that monoclinic Zirconia allows the temperature dependence of the phonon mean free path to operate while cubic Zirconia does not. Since Zirconia is partially monoclinic at lower temperatures, this also helps to explain the initial rapid decent in diffusivity. At higher temperatures where photons should become the dominant thermal transport carriers, the thermal diffusivity of single crystals at 100% theoretical density has been shown to increase again.[13] Since our YSZ is polycrystalline and quite porous, this increase is probably not observed due to the scattering of photons by grain boundaries and pores.

In order to check the quantitative accuracy of our thermal transport properties, these calculated diffusivity values should be compared with published ones. As mentioned previously, Pawlowski and Fauchais have published thermal diffusivity data for YSZ with 7.25%(wt.) Y_2O_3 and a porosity of 8%.[10] Lenling et al. provides thermal diffusivity data for theoretical full-density 8%(wt.) Yttria / 1.7%(wt.) Hafnia / 0.4%(wt.) Silica stabilized Zirconia.[14] Touloukian also provides thermal diffusivity data taken from several experiments. The data was taken from experiments on pure Zirconia and Magnesia stabilized Zirconia.[9]

Figure A4 shows a plot of our calculated diffusivity values and these published diffusivity values versus temperature. Since the measurements were all taken from YSZ samples with similar but not identical structures to the YSZ of interest, caution must be taken in making comparisons. One assuring feature of the plot is that all the data lies within one order of magnitude. Second, notice that the Pawlowski and Fauchais data, which matches our YSZ closely in both composition and porosity, agrees relatively well with our calculated values. The plot also shows us that the data sets from Lenling et al. and Touloukian agree less and less closely; however, their measurements were taken on YSZ which gets progressively different from ours with respect to stabilizer content. A final look at the graph shows us that all the published data sets seem to agree with the temperature dependence of our calculate values. Unfortunately, the published data stops around 1200K and cannot confirm higher temperature dependencies.

This shall conclude our discussion of properties for solid YSZ. Attention shall now be turned to the properties of molten YSZ. No density data for molten YSZ or pure Zirconia was uncovered during this investigation. Due to the lack of data for liquid Zirconia, Fantassi et al. assumed a constant value of 5.7 g/cm^3 for their research.[16] For this research it shall be assumed that the density of molten YSZ at its melting point is its theoretical density, 6.0 g/cm^3. Typically, the density of a liquid varies according to the relation:

$$\rho=\rho_o[1-\beta(T-T_o)]$$

Figure A4: Thermal Diffusivity versus Temperature Comparisons

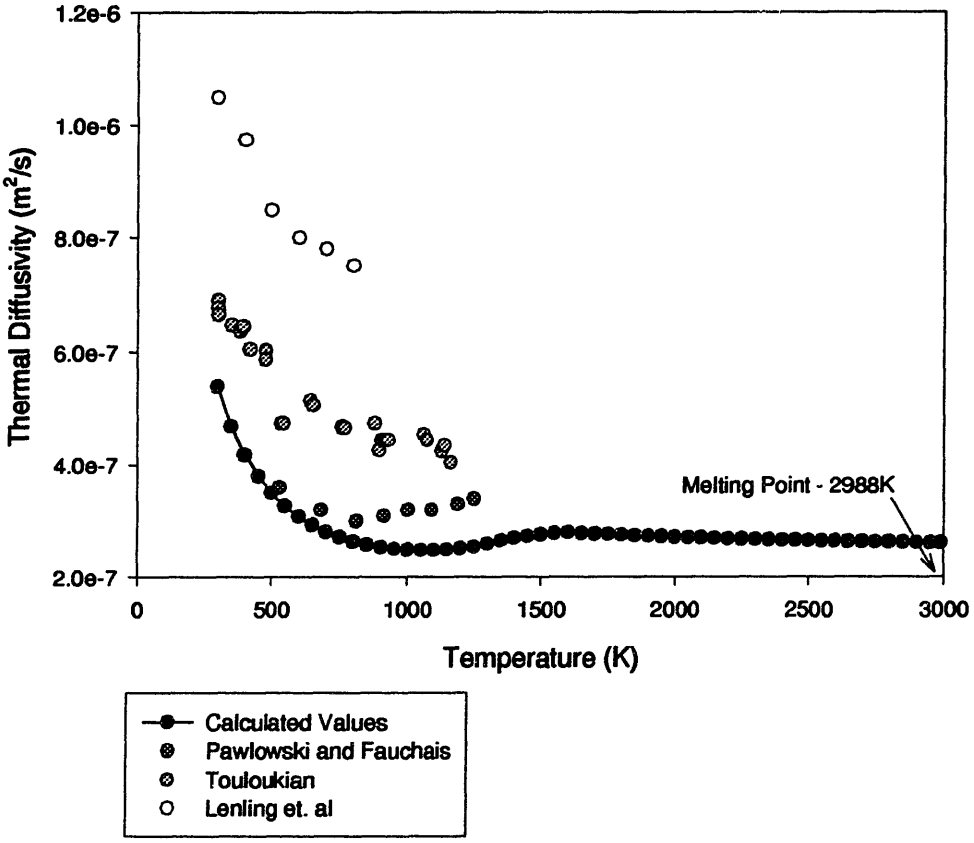

where ρ is the density at temperature T, ρ_o is the density at temperature T_o and β is the thermal expansion coefficient. The thermal expansion coefficient of YSZ can be approximated by substituting density data for molten Alumina. The relationship between Alumina's molten density and temperature is quite linear and provides us with a constant thermal expansion coefficient of 3.88E-4 K^{-1}.[17]

Viscosity data for molten Zirconia and YSZ was also unavailable. Fantassi et al. assumed Zirconia's absolute viscosity, m, to be a constant 4.0E $^{-2}$ kg/ms for their research.[16] Our research shall use Alumina's viscosity data which somewhat agrees with their assumption. Kawai has published the viscosity of Alumina in tabular format [17]:

Table A2: Absolute Viscosity Data for Alumina			
Temperature (K)	2323	2373	2473
Viscosity (kg/ms)	0.0417	0.0380	0.0302

where 2323K is the melting point of Alumina. Assuming that YSZ's melting point viscosity is the same as Alumina's at its melting point, and that their temperature dependence is similar the following could be proposed:

Table A3: Proposed Viscosity Data for 7%(wt.) Y2O3 stabilized ZrO2			
Temperature (K)	2988	3038	3088
Viscosity (kg/ms)	0.0417	0.0380	0.0302

This data can be fitted with an Arrhenius type relation as suggested by Geiger and Poirier[18] to produce the following expression for viscosity as a function of temperature:

$$\mu(T) = 3.24E^{-5} \exp(2.83E^{4}/T). \quad [kg/ms]$$

where μ is viscosity and T is absolute temperature. This expression provides our best approximation for the temperature dependence of YSZ's viscosity. When modeling molten YSZ with constant properties, the melting point value of 0.42 kg/ms shall be used.

Surface tension, σ, is another property lacking data for Zirconia and YSZ. Again data for molten Alumina is substituted. Kawai has published two items that are useful in estimating YSZ's surface tension. The first item is a plot of Alumina's surface tension versus temperature over the range 2080°C (30°C above its melting point) to 2710°C. Over this wide range of temperatures the relationship shown is quite linear. Thus, by determining the slope of Alumina's surface tension versus temperature relationship, an approximate value for $d\sigma/dT$ can be determined. This value is $-3.095E^{-4}$ N/mK. Since this research will be interested in surface tension gradients as opposed to absolute surface tension values, the value of $d\sigma/dT$ will be sufficient information.

None of the thermal transport properties of molten YSZ were uncovered during this investigation. Their values can be approximated by extrapolating to YSZ's melting point from the data available for its solid state. The conductivity data will also be corrected to represent a fully dense material using the Bruggeman model. This provides us with the following estimates:

Table A4: Estimates for YSZ's Molten Thermal Transport Properties	
Thermal Conductivity, k	2.7 W/mK
Specific Heat, c_p	$1.4E^{3}$ J/kgK
Thermal Diffusivity, a	$2.5E^{-7}$ m^2/s

And finally, an estimate for the emissivity of molten YSZ will be required for calculations of radiative heat transfer. Touloukian has published data for solid state Zirconia for temperatures up to 2811K where the emissivity has been measured to be 0.475. Meanwhile, Lillquist suggests that the emissivity of molten YSZ is greater than 0.6. We shall use his recommended value of 0.65.[19]

Thermophysical Property Summary

Figure 5 summarizes the thermophysical properties of Yttria stabilized Zirconia in a concise format. From the discussion above it is obvious that many of YSZ's general and solid state properties are well studied and understood. Conversely, the properties of molten YSZ and even pure Zirconia are widely unknown.

Figure 5: Summary of YSZ Properties of Interest:

General Properties:
Composition: 7%(wt.) Y_2O_3, 93%(wt.) ZrO_2
Melting Point: T_{mp}=2988K
Approximate Liquidus: T_l=2951K, Approximate Solidus: T_s=3026K
Zirconia's Vapor Pressure: $\log(P_{atm}) = -4.1176E4/T + 10.088$
Zirconia's Heats of Melting and Vaporization: h_{sl}=706.3 kJ/kg, h_{lg}=5069.6 kJ/kg

Solid Phase:
Theoretical Density: ρ=6.0 g/cm^3
Porosity: ω=25% - 40%
Thermal Conductivity:

$k(T) = 1.241 - 1.284E^{-3}T + 6.186E^{-7}T^2$ [W/mK] (300K<T<1250K)
$k(T) = 4.341E^{-4}T + 5.98E^{-2}$ [W/mK] (1250K<T<2988K)

Specific Heat:

$c_p(T) = -61.028 + 2.627T - 3.847E^{-3}T^2 + 2.558E^{-6}T^3$
$-7.526E^{-10}T^4 + 8.288E^{-14}T^5$ [J/kgK] (50K<T<1600K)
$c_p(T) = -47.44 + 0.4723T$ [J/kgK] (1600K<T<2988K)

Liquid Phase:
Thermal Expansion Coefficient: $\beta \approx 3.88E\text{-}4\ K^{-1}$
Viscosity: $\mu(T) \approx 3.24E^{-6} \exp(2.83E^4/T)$. [kg/ms]
Surface Tension Coefficient: $d\sigma/dT \approx -3.095E\text{-}4$ [N/mK]
Thermal Conductivity: $k \approx 2.7$ W/mK
Specific Heat: $c_p \approx 1.4E^3$ J/kgK
Thermal Diffusivity: $\alpha \approx 2.5E^{-7}$ m^2/s
Emissivity: $\varepsilon \approx 0.65$

Note for the above expressions:
T = Temperature (K)

Appendix B:

Order of Magnitude Analysis of the Melt Pool

The objective of this analysis is to estimate the relative importance of buoyancy driven flow and surface tension driven flow within the melt pool. We shall begin by estimating the radial velocities to be expected in a melt pool driven purely by buoyancy. We must examine the equations of conservation of mass and momentum. Conservation of mass would be written for our axisymmetric system as follows:

$$\frac{1}{r}\frac{\partial}{\partial r}(ru_r)+\frac{\partial u_z}{\partial z}=0$$

where each of the terms could estimated to an order of magnitude by:

$$\frac{1}{r}\frac{\partial}{\partial r}(ru_r)\sim\frac{1}{L}\frac{1}{L}LU_r=\frac{U_r}{L}$$
$$\frac{\partial u_z}{\partial z}\sim\frac{U_z}{\delta}$$

where L, δ, U_r, and U_z are a characteristic radial dimension, axial dimension, radial velocity, and axial velocity, respectively. Substituting and solving for U_r:

$$U_r\sim\frac{L}{\delta}U_z$$

Now we can analyze conservation of momentum:

$$\rho_o\left[\frac{\partial u_z}{\partial t}+u_r\frac{\partial u_z}{\partial r}+u_z\frac{\partial u_z}{\partial z}\right]=\frac{-\partial p}{\partial z}+\mu\left[\frac{1}{r}\frac{\partial}{\partial r}\left(r\frac{\partial u_z}{\partial r}\right)+\frac{\partial^2 u_z}{\partial z^2}\right]+(\rho-\rho_o)g$$

where the terms, $\frac{\partial u_z}{\partial t}$ and $\frac{-\partial p}{\partial z}$, are small and can be neglected immediately.

The remaining terms could be estimated to an order of magnitude by:

$$u_r\frac{\partial u_z}{\partial r}\sim U_r\frac{\delta}{L}\frac{U_r}{L}=\frac{\delta}{L}\frac{U_r^2}{L}$$
$$u_z\frac{\partial u_z}{\partial z}\sim\frac{\delta^2}{L^2}\frac{U_r^2}{\delta}=\frac{\delta}{L}\frac{U_r^2}{L}$$
$$\frac{1}{r}\frac{\partial}{\partial r}\left(r\frac{\partial u_z}{\partial r}\right)\sim\frac{1}{L}\frac{1}{L}\left(L\frac{\delta}{L}\frac{U_r}{L}\right)=\frac{\delta}{L}\frac{U_r}{L^2}$$
$$\frac{\partial^2 u_z}{\partial z^2}\sim\frac{\delta}{L}\frac{U_r}{\delta^2}$$
$$(\rho-\rho_o)g\sim\rho\beta\Delta T_z g$$

where ΔT_z is a characteristic axial temperature difference and the remainder of the symbols have already been defined. If ΔT_z were chosen to represent the temperature difference between the melt pool's surface and melting front, a value of 100K would correspond with typical industrial measurements of melt pool surface temperatures.

Note that the two terms within the brackets on the right hand side of the conservation equation are similar except that the first varies as $1/L^2$ and the second varies as $1/\delta^2$. Experience tells us that the pool is much wider than it is deep ($\delta << L$) so the first term can be neglected. Plugging in the remaining terms, our expression for momentum conservation becomes:

$$\rho\left[\frac{\delta}{L}\frac{U_r^{\,2}}{L}\right] \sim \mu\left[\frac{\delta}{L}\frac{U_r}{\delta^2}\right] + \rho\beta\Delta T_z g$$

If we assume that the flow is inviscid and neglect the first term on the right hand side of the equation, the following must be true:

$$\frac{\rho\dfrac{\delta}{L}\dfrac{U_r^{\,2}}{L}}{\mu\dfrac{\delta}{L}\dfrac{U_r}{\delta^2}} = \frac{\delta}{L}\frac{\rho U_r \delta}{\mu} >> 1$$

If this is the case, then we can solve for U_r and plug in the appropriate values as follows:

$$U_r \sim \sqrt{\frac{L}{\delta}\beta\Delta T_z g L} \sim .01 \text{ m/s}$$

Checking the above condition for inviscid flow we find:

$$\frac{\delta}{L}\frac{\rho U_r \delta}{\mu} \sim 0.1$$

which does not satisfy our condition for inviscid flow. At the other extreme, we could assume that the flow is highly viscous and neglect the term on the left hand side of the equation. For this to be true the following must be observed:

$$\frac{\rho\dfrac{\delta}{L}\dfrac{U_r^{\,2}}{L}}{\mu\dfrac{\delta}{L}\dfrac{U_r}{\delta^2}} = \frac{\delta}{L}\frac{\rho U_r \delta}{\mu} << 1$$

If this condition is satisfied, we can solve for U_r and plug in the appropriate values as follows:

$$U_r \sim \frac{L}{\delta}\frac{\rho\beta\Delta T_z g\delta^2}{\mu} \sim .01 \text{ m/s}$$

Checking the above condition for highly viscous flow we again find:

$$\frac{\delta}{L}\frac{\rho U_r \delta}{\mu} \sim 0.1$$

which is certainly less than unity but not exactly much less than unity. Therefore, the flow should probably not be approximated as either inviscid or highly viscous. However, in either extreme we found that U_r was of the order .01 m/s. As a result, we shall say that the characteristic radial velocity due to buoyancy forces is of the order .01 m/s regardless of the relative importance of the inertial and viscous terms in the momentum conservation equation.

Obtaining an estimate for the characteristic radial velocity in a melt pool driven purely by surface tension gradients is much simpler but the result is slightly less satisfying. The boundary condition for shear stress on the melt pool's free surface is written as follows:

$$\mu\frac{\partial u_r}{\partial z} = \frac{\partial\sigma}{\partial T}\frac{\partial T}{\partial r}$$

Each of the terms in this boundary condition may be estimated to an order of magnitude as follows:

$$\mu\frac{\partial u_r}{\partial z} \sim \mu\frac{U_r}{\delta}$$

$$\frac{\partial\sigma}{\partial T}\frac{\partial T}{\partial r} \sim \frac{\partial\sigma}{\partial T}\frac{\Delta T_r}{L}$$

where ΔT_r is a characteristic radial temperature difference.

Providing an value for this term is somewhat subjective. We have selected 100K to represent ΔT_z, which could be thought of as the temperature difference between the center of the melt pool's surface and the center of the melt pool's melting front. We could select ΔT_r to represent the temperature difference between the center and edge of the melt pool's surface. Since the temperature at the edge of the melt pool's surface must be above the melting temperature of the material under normal coating conditions (otherwise the electron-beam would be burrowing a hole in the middle of the ingot) we

know that ΔT_r must be bounded by ΔT_z. Under an electron-beam scanning pattern that provide nearly constant heat flux across the pool surface, ΔT_r should be, say, ~10K. Switching to a scanning pattern that provides a gaussian distribution of heat flux, ΔT_r should begin to approach ~100K as the standard deviation of the distribution increases.

Inserting the approximations for each term in the boundary condition, solving for U_r, and plugging in appropriate values yields:

$$U_r \sim \frac{\delta}{L}\frac{\partial \sigma}{\partial T}\frac{\Delta T_r}{\mu} \sim .01 \text{ m/s - } .1 \text{ m/s}$$

where the lower bound on U_r corresponds to the lower bound on ΔT_r (10K) and the upper bound on U_r corresponds to the upper bound on ΔT_r (100K).

Recall that our order of magnitude analysis showed that the characteristic velocity in a melt pool stirred purely by buoyancy is ~.01 m/s. Thus, when the heat flux through the melt pool's surface is relatively uniform, we find that the effects of buoyancy and surface tension gradients are of equal importance. In the case where a Gaussian distribution of heat flux has caused the edge of the melt pool to drop in temperature significantly (such that the edge of the pool is nearly solidified), we find that surface tension gradients become slightly more important in driving flow within the melt pool.

References:

1 Gerard, Curtis F. and Wheatley, Patrick O., Applied Numerical Analysis, Addison-Wesley Publishing Company, 1994, p. 41.

2 Ryshkewitch, Eugene, Oxide Ceramics, Academic Press, 1960.

3 Musikant, Soloman, What every engineer should know about Ceramics, Marcel-Dekker, Inc., 1991

4 Margrave, John L., The Characterization of High Temperature Vapors, John Wiley & Sons, Inc., 1967.

5 Sata, Toshiyuki, High Temperature Vapourisation from Ceramic Materials, Proceedings of the Silver Jubilee Commemoration Seminar of Indian Institute of Technology on Recent Advances in Materials Research, A.A. Balkema, 1984.

6 Barin, Ihsan, Thermochemical Data of Pure Substances, 1993.

7 JANAF Thermochemical Tables, 1974.

8 Sanoaob, Trans Tech, Inc., Adamstown, MD, telephone conversation.

9 Touloukian, Y.S., Thermophysical Properties of Matter, 1970-79.

10 Pawlowski, L. and Fauchais, P., "Thermal transport properties of thermally sprayed coatings," International Materials Review, 1992, Vol. 37, No. 6.

11 Hasselman et al., "Thermal Diffusivity and Conductivity of Dense Polycrystalline ZrO2 Ceramics: A Survey," Ceramic Bulletin, 1987, Vol. 66, No. 5.

12 Hague, D., Unpublished data.

13 Youngblood et al., "Thermal Diffusivity of Partially and Fully Stabilized (Yttria) Zirconia Single Crystals," Journal of the American Ceramic Society, 71 [4] 255-60 (1988).

14 Lenling et al., "Thermal Coating Development for Impulse Drying," Journal of Thermal Spray Technology, June 1993, Vol. 2(2).

15 Kleitz et al., "Determination of electronic conductivites and ionic domains of ZrO_2-Y_2O_3 by semipermeability measurements," First International Conference on the Science and Technology of Zirconia, Cleveland, Ohio, June 16-18 1980.

16 Fantassi et al., "Infllluence of the Velocity of Plasma Sprayed Particles on the Splat Formation," Proceedings of the 1993 National Thermal Spray Conference, Anaheim, CA, June 7-11 1993.

17 Kawai, Yasuji and Shiraishi, Yutaka, Handbook of Physico-chemical Properties at High Temperatures, Iron and Steel Institute of Japan, 1988.

18 Geiger G.H. and Poirier D.R., Transport Phenomena in Metallurgy, Addison-Wesley Publishing Company, 1973.

19 Lillquist, R.D., Unpublished data.